DIPLOMARBEIT

Quantum Entanglement Distribution and Routing over an Operator's Urban Fiber Infrastructure

ausgeführt am

Institut für Photonik
TU Wien

unter der Anleitung von

Univ.Prof. Mag.rer.nat. Dr.rer.nat.
Karl UNTERRAINER

Dr.-Ing.
Matheus RIBEIRO SENA
(T-Labs, Deutsche Telekom)

durch

Thomas Rieser
Matrikelnummer: 01532096

Wien, am 2. September 2025

Kurzfassung

Diese Arbeit untersucht die Übertragung polarisationsverschränkter Photonen im O-Band über ein bereits existierendes Glasfasernetzwerk der Deutschen Telekom AG in Berlin. Im Folgenden werden die Einflüsse des dynamischen Wechseln der Übertragungsstrecken sowie das gleichzeitige Übertragen klassischer optischer Nachrichtensignale im C-Band analysiert. Im Gegensatz zu anderen Studien, die unter stabilen Laborbedingungen durchgeführt wurden, werden hier Experimente in einer realen Umgebung unter Verwendung einer großstädtischen Glasfaserinfrastruktur durchgeführt. Solche Glasfaserinfrastrukturen sind zusätzlichen Herausforderungen ausgesetzt. Durch Umwelteinflüsse wie mechanischen Stress und Temperaturschwankungen wird die Qualität der Übertragung verschränkter Photonen beeinträchtigt. Das primäre Ziel dieser Arbeit ist es, verschränkungsbasierte Quantenkommunikation trotz solch unvorhersehbarer Einflüsse anhand experimenteller Messungen zu demonstrieren.

Die Experimente wurden in vier Phasen unterteilt, deren Ziel es war, dynamische Routing-Operationen zu realisieren und die Koexistenz von klassischen optischen Nachrichtensignalen und Quantensignalen auf derselben Glasfaser zu demonstrieren. Als Erstes wurden die verfügbaren Übertragungsfasern mittels optischer Zeitbereichsreflektometrie charakterisiert. Anschließend wurden polarisationskodierte verschränkte Photonen über das Netzwerk übertragen und mittels der Bellschen Ungleichung die Verschränkheit nachgewiesen. In der zweiten Phase wurde mithilfe eines steuerbaren optischen Schalters der Wechsel der Übertragungsstrecke analysiert. Eine Langzeitanalyse wurde unter verschiedensten Bedingungen über mehrere Stunden bzw. Tage durchgeführt. Abschließend wurde die Auswirkung von optischen Nachrichtensignalen im C-Band auf das Quantensignal im O-Band untersucht.

Die Ergebnisse zeigen, dass eine quantenverschränkte Kommunikation über eine Distanz von bis zu 100 km in diesem Glasfasernetzwerk möglich ist. Die Experimente ermöglichten auch dynamische Routingprozess, unter der Verwendung von automatisierter Polarisationskompensation. Individuelle Streckenabhängige Polarisationsverschiebungen würden ansonsten manuelle Kalibrierungsroutinen für jeden Streckenwechsel erfordern. Die Langzeitanalyse bestätigt eine zuverlässige Detektion der Verschränkung über einen längeren Zeitraum. Die Koexistenz von Quantensignalen und klassischen optischen Nachrichtensignalen ist zwar möglich, jedoch beeinträchtigt dies die Detektion. Verschiedene Parameter für das klassische Signal, wie die optische Leistung und die spektrale Platzierung, beeinflussen die Messung der Verschränktheit. Die gewonnen Ergebnisse stellen einen bedeutenden Fortschritt zur Integration von Quantenkommunikationstechnologien in bestehende Telekommunikationsnetzwerke dar und tragen zur Vision eines zukünftigen Quanteninternets bei.

Abstract

This thesis investigates the feasibility of distributing, routing, and multiplexing O-band polarization-entangled photons with C-band classical light over an urban field-deployed optical fiber network owned by Deutsche Telekom AG in Berlin. In contrast to other studies carried out under stable laboratory conditions, this work is conducted in a real-world environment using existing metropolitan optical fiber infrastructure. Such field-deployed optical fibers face additional challenges from environmental factors such as mechanical stress and temperature fluctuations, which can compromise the quality of the entanglement distribution. Therefore, this work demonstrates with practical measurements that entanglement-based quantum communication is still feasible in such an unpredictable environment.

The experiments described along this text were divided into four phases. These aimed at achieving dynamic routing operations and at demonstrating the co-propagation of classical light and quantum signals. First, the available transmission distances were characterized by optical time-domain measurements. Then polarization-entangled photon pairs were distributed through fibers to obtain a measurable violation of the Bell inequality. Second, the impact of dynamic routing using a controllable optical switch was analyzed. A long-term analysis was conducted over several days by measuring the Bell parameter and fidelity under various path switching conditions. Finally, the influence of co-propagating C-band classical light on the O-band quantum signal was examined.

The presented results show that robust quantum entanglement can be maintained up to a distance of 100 km over field-deployed fiber infrastructure. The experiment also validates a dynamic entanglement routing process with an automated polarization compensation mechanism. Furthermore, long-term evaluation over hours confirmed stable operation in an urban network scenario. Finally, the coexistence of quantum and classical light is possible, but it comes at the cost of reliably detecting entanglement. Various transmission parameters, such as optical power and spectral allocation, have different influences on entanglement measurements. The outcomes derived from this study represent a meaningful step toward the integration of quantum communication technologies into existing telecom networks and contribute to the vision of a future Quantum Internet.

Eidesstattliche Erklärung

Ich erkläre an Eides statt, dass ich die vorliegende Diplomarbeit selbstständig und ohne fremde Hilfe verfasst, andere als die angegebenen Quellen und Hilfsmittel nicht benutzt bzw. die wörtlich oder sinngemäß entnommenen Stellen als solche kenntlich gemacht habe. Hilfsmittel der künstlichen Intelligenz wurden nur verwendet, um sprachliche Formulierungen und Zeichensetzung Korrektur zu lesen und gegebenenfalls zu verbessern.

Wien, am 2. September 2025

Thomas Rieser

Contents

1 Introduction

This chapter provides an overview of the motivation, research focus, and state of the art concerning quantum networks. It begins by highlighting the importance of entanglement distribution for the Quantum Internet. It also addresses the challenges when deploying such systems in real-world telecommunication network environments. Based on this motivation, key research questions are formulated to guide the investigation. Finally, this chapter concludes with a review of related work on quantum networks and discusses how this study is positioned within that context.

1.1 Motivation

The Quantum Internet [1] marks the next major step in the evolution of telecommunication networks. However, its realization critically depends on enabling efficient quantum communication over long distances. For instance, applications such as quantum key distribution (QKD) [2], quantum repeaters (QR) [3], quantum sensing [4], and time synchronization [5] rely on the efficient distribution of photonic entanglement. Consequently, quantum entanglement distribution has become a foundational capability for quantum networks. While laboratories have already demonstrated high-fidelity entanglement distribution, real-world deployments introduce new challenges. Environmental factors such as mechanical stress on the fiber (e.g. bending, vibrations) and temperature fluctuations induce a change of birefringence, which in turn causes polarization drifts [6]. This unpredictable and unavoidable behavior of polarization drift becomes relevant as quantum networks grow in complexity, especially with the routing and switching of entangled photons in multi-path topologies common in real-world networks .

Telecommunication operators are interested in using their field-deployed optical fiber network to create additional revenue streams. The integration of quantum communication technologies, for instance, can improve the security of the network to the quantum level, which represents an innovation with a strong potential for customer applications in an era, where quantum computers are no longer a promise but a reality. Therefore, the practical implementation of quantum technologies into existing infrastructure requires continued research and technological refinement in order to support a stable entanglement distribution without compromising classical data transmission. The challenge is to ensure efficient entanglement distribution with high rates of coincidences per second, stable fidelity over days, and high network uptime [7].

1.2 Research Questions

The intention of this research is to demonstrate the feasibility of efficient entanglement distribution over various path lengths by dynamically switching across existing optical telecommunication infrastructure with commercially available state-of-the-art optical devices. Furthermore, the research also considers how C-band (1530–1565 nm) classical light impacts the transmission of an O-band (1260–1360 nm) quantum signal. Based on these goals, this study addresses the following questions:

I. What are the practical distance limits for polarization-entangled photon distribution in the deployed urban optical fiber network?

II. How does dynamic routing/switching affect polarization compensation?

III. How stable is entanglement fidelity and Bell parameter over multiple days in a real-world fiber optical network, particularly during continuous path switching?

IV. How does the coexistence of classical optical signals affect the entanglement and stability of polarization-entangled photons in optical fiber networks?

1.3 State of the Art

Significant progress has been made in the experimental distribution of polarization-entangled photons across optical fiber infrastructures. Table 1 offers an overview of different publications that have successfully demonstrated quantum entanglement distribution in various settings.[1] In summary, Table 1 provides key parameters of the selected studies results, highlighting experimental settings (e.g., laboratory or urban setups), fiber length, achieved fidelity, operating wavelengths, presence of coexisting classical light signals, and duration of the experiments [8]. The fidelity metric (in %) is an indicator of the entanglement quality and measures how close the observed quantum state matches the ideal entangled state [9]. Most existing works have been conducted either in controlled laboratory environments or urban fiber networks, with fiber lengths ranging from about 14 km up to 66 km.

While some experiments operate without classical light signals, others investigate coexistence scenarios with classical channels. The duration of stable entanglement distribution varies widely, from hours in laboratory tests to several days in urban deployments, indicating progress toward long-term operation.

Reference	Location	Setting	Fiber (km)	Fidelity (%)	Wavelengths (nm)	Classical Light (nm)	Duration
[10]	Geneva, CH	Laboratory	50	~ 80	1310	1534	hours
[11]	Singapore, SG	Laboratory	50	92.5-97	586, 1310	-	-
[12]	Chicago, US	Laboratory	30.2	> 90	1290-1310	1547	-
[13]	Shandong, CN	Urban	66	-	1310	1490, 1538	-
[14]	Stuttgart, DE	Urban	35.8	94.5	780, 1515	-	days
[15]	Brooklyn, US	Urban	34	99	795, 1324	-	15 days
[16]	Saarbrücken, DE	Urban	14	> 98	854, 1550	-	-

Table 1: Performance metrics of quantum entanglement distribution deployments.

[1] To show comparable results to this work, Table 1 focused on bicromatic O-band distribution.

Compared to these studies, this work's contribution aims to explain quantum entanglement distribution by dynamically switching across existing field-deployed fiber infrastructure. In particular, the impact of dynamic routing on polarization compensation and the effects of simultaneous classical data transmission.

2 Theoretical Background

This chapter provides the theoretical background necessary to understand the experimental results presented later in this work and is divided into four sections. Each addresses a key concept relevant to the analysis and interpretation of the data and results.

The first section introduces the concept of qubits, especially photonic qubits, and explains how polarization encoding is used for quantum communication. The second section explains the basics for understanding quantum entanglement. The third section combines qubits and entanglement in the form of Bell states. Finally, the fourth section discusses the characterization of entanglement using the Clauser–Horne–Shimony–Holt inequality.

Together, these sections form the framework for interpreting the upcoming experimental results.

2.1 Qubits

A qubit represents the quantum equivalent of the classical bit. While the classical bit is typically represented as 0 and 1 in digital communication systems, the qubit supports a much richer information structure. The term qubit was first used in 1995 by Benjamin Schumacher in his paper on quantum coding [17].

The qubit is the fundamental element of quantum computation and quantum communication. Its unique properties come from the principles of quantum superposition and entanglement with other qubits. While the classical bit, encoded in a binary format, can only represent the information in one of two states at the same time, a qubit can exist in a superposition of states [18]. This means that it can be in a linear combination of two computational basis states $|0\rangle$ and $|1\rangle$ simultaneously. The notation $|v\rangle$ refers to Dirac notation [19], which represents a vector in a complex Hilbert space $\mathcal{H}$. Mathematically, a pure qubit state is described as a normalized vector $|\psi\rangle$ in a two-dimensional Hilbert space:

$$|\psi\rangle = \alpha|0\rangle + \beta|1\rangle,$$

where α,$\beta \in \mathbb{C}$ represent the complex amplitudes of the computational basis states $|0\rangle$ and $|1\rangle$, respectively, such that $|\alpha|^2 + |\beta|^2 = 1$.

Oftentimes, the state of a qubit is geometrically represented on the Bloch sphere [20]. In this model, any pure qubit state can be expressed as a point on the surface of a unit sphere in a three-dimensional space. The north and south poles of the Bloch sphere correspond to the computational basis states $|0\rangle$ and $|1\rangle$, respectively. For a better understanding of the Bloch sphere, a common representation is performed by using polar coordinates, where the qubit is described with two spherical angles θ and ϕ, that is:

$$|\psi_{\theta,\phi}\rangle = \cos\left(\frac{\theta}{2}\right)|0\rangle + e^{i\phi}\sin\left(\frac{\theta}{2}\right)|1\rangle,$$

where θ ranges from 0 to π ($\theta \in [0, \pi]$) and determines the latitude, while ϕ ranges from 0 to 2π ($\phi \in [0, 2\pi]$) and determines the longitude of the point. This is illustrated in Figure 1.

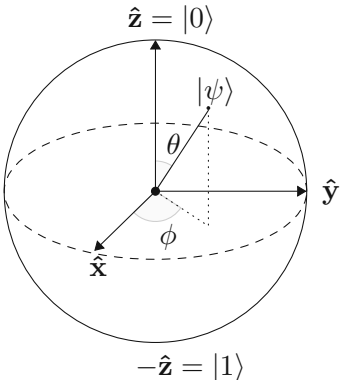

Figure 1: Bloch sphere representation of a single-qubit pure state $|\psi\rangle$, parameterized by spherical coordinates (θ, ϕ). $\hat{\mathbf{x}}$, $\hat{\mathbf{y}}$, and $\hat{\mathbf{z}}$ represent the coordinate axis of the Bloch sphere.

After exploring the Bloch sphere as a model for qubit representation, attention is now directed to the specific case of photonic qubits.

Photonic Qubits and Polarization Encoding

Photons follow the rules of quantum mechanics, which makes them suitable for use as qubits. In that sense, there are various ways to realize photonic qubits, such as time-bin [21], frequency-bin [22], or polarization-encoding [8]. In this work, the focus is on polarization-encoded qubits as they are easier to manipulate and to measure using standard optical components. Additionally, polarization qubits exhibit high compatibility with quantum memories [23].

To provide a foundational understanding, a revisit of the Jones notation follows [24]. Consider a plane wave propagating in the positive z-direction. The electric field $\mathbf{E}(z, t)$ can be written as:

$$\mathbf{E}(z,t) = \begin{bmatrix} E_{0\mathrm{x}} \cos(\omega t - kz) \\ E_{0\mathrm{y}} \cos(\omega t - kz + \Delta\phi) \end{bmatrix}.$$

Here, $E_{0\mathrm{x}}$ and $E_{0\mathrm{y}}$ denote the amplitudes of the electric field components along the orthogonal x and y basis vectors, respectively. The parameter $\Delta\phi$ represents the relative phase between these components. The term $(\omega t - kz)$ encodes the oscillation in time and the propagation in space, where ω is the angular frequency, t is the time, k is the wave number and z the coordinate along the direction of propagation.

In the Jones formalism, it is assumed that the light is coherent, meaning the relative phase remains constant in time ($\Delta\phi = \text{const.}$). The electric field can be written as the real part of a complex vector, factoring out the common space-time dependence:

$$\mathbf{E}(z,t) = \Re\left\{e^{i(\omega t - kz)} \begin{bmatrix} E_{0\mathrm{x}} \\ E_{0\mathrm{y}} e^{i\Delta\phi} \end{bmatrix}\right\} = \Re\left\{e^{i(\omega t - kz)} \mathbf{J}'\right\},$$

where $\mathbf{J}'$, the unnormalized Jones vector, is defined as:

$$\mathbf{J}' := \begin{bmatrix} E_{0\mathrm{x}} \\ E_{0\mathrm{y}} e^{i\Delta\phi} \end{bmatrix}.$$

Normalizing the previous equation with the total field amplitude, the Jones vector $\mathbf{J}$ becomes:

$$\mathbf{J} = \frac{\mathbf{J}'}{\sqrt{E_{0\mathrm{x}}^2 + E_{0\mathrm{y}}^2}}.$$

The electric field then takes the compact form:

$$\mathbf{E}(z,t) = \Re\left\{\sqrt{E_{0\mathrm{x}}^2 + E_{0\mathrm{y}}^2}\, e^{i(\omega t - kz)}\, \mathbf{J}\right\}.$$

Finally, the Jones vector can be written as:

$$\mathbf{J} = \frac{1}{\sqrt{E_{0\mathrm{x}}^2 + E_{0\mathrm{y}}^2}} \begin{bmatrix} E_{0\mathrm{x}} \\ E_{0\mathrm{y}} e^{i\Delta\phi} \end{bmatrix} = \begin{bmatrix} \cos(\alpha) \\ \sin(\alpha) e^{i\Delta\phi} \end{bmatrix},$$

where $\alpha = \arctan(E_{0\mathrm{y}}/E_{0\mathrm{x}})$.

The qubit is described in the computational basis $|0\rangle$ and $|1\rangle$, which consists of the two orthogonal basis vectors. When written in vector notation, these basis states directly resemble the familiar Jones vector. In polarization-encoded quantum systems, computational basis vectors are typically represented by horizontal $|\mathrm{H}\rangle$ and vertical $|\mathrm{V}\rangle$ polarization states. The computational basis states can be mapped to the polarization states as follows:

$$|0\rangle = \begin{bmatrix} 1 \\ 0 \end{bmatrix} = |\mathrm{H}\rangle, \quad |1\rangle = \begin{bmatrix} 0 \\ 1 \end{bmatrix} = |\mathrm{V}\rangle.$$

For polarization-encoded qubits, there are additional states to explore. These include diagonal $|\mathrm{D}\rangle$, antidiagonal $|\mathrm{A}\rangle$, right-circular $|\mathrm{R}\rangle$ and left-circular $|\mathrm{L}\rangle$ polarization states. In terms of the horizontal $|\mathrm{H}\rangle$ and vertical $|\mathrm{V}\rangle$ polarization basis, the above-mentioned states are defined as follows:

$$\begin{aligned}
|\mathrm{D}\rangle &= \tfrac{1}{\sqrt{2}}\left(|\mathrm{H}\rangle + |\mathrm{V}\rangle\right) &&= \tfrac{1}{\sqrt{2}} \begin{bmatrix} 1 \\ 1 \end{bmatrix}, \\
|\mathrm{A}\rangle &= \tfrac{1}{\sqrt{2}}\left(|\mathrm{H}\rangle - |\mathrm{V}\rangle\right) &&= \tfrac{1}{\sqrt{2}} \begin{bmatrix} 1 \\ -1 \end{bmatrix}, \\
|\mathrm{R}\rangle &= \tfrac{1}{\sqrt{2}}\left(|\mathrm{H}\rangle + i|\mathrm{V}\rangle\right) &&= \tfrac{1}{\sqrt{2}} \begin{bmatrix} 1 \\ i \end{bmatrix}, \\
|\mathrm{L}\rangle &= \tfrac{1}{\sqrt{2}}\left(|\mathrm{H}\rangle - i|\mathrm{V}\rangle\right) &&= \tfrac{1}{\sqrt{2}} \begin{bmatrix} 1 \\ -i \end{bmatrix}.
\end{aligned}$$

The description of photon qubits can be extended using the Stokes-Mueller formalism [25], which originates from classical optics and provides a complete description of the polarization state. In this formalism, any polarization state can be described by a four-dimensional, real-valued Stokes vector:

$$\mathbf{S} = \begin{bmatrix} S_0 \\ S_1 \\ S_2 \\ S_3 \end{bmatrix}, \quad \begin{cases} S_0 = |E_\mathrm{x}|^2 + |E_\mathrm{y}|^2 \\ S_1 = |E_\mathrm{x}|^2 - |E_\mathrm{y}|^2 \\ S_2 = 2\Re\left\{E_\mathrm{x}E_\mathrm{y}^*\right\} \\ S_3 = 2\Im\left\{E_\mathrm{x}E_\mathrm{y}^*\right\} \end{cases},$$

where S_0 represents the total power, S_1 corresponds to the difference between the magnitude of the horizontal and vertical polarization components, S_2 represents the difference between the magnitude of the diagonal and antidiagonal components, and S_3 captures the difference between the magnitude of the right and left circular components. These parameters can be directly measured in classical optics using appropriate polarizers and detectors. If the Stokes vector is normalized so that $S_0 = 1$, the values S_1, S_2, S_3 describe the polarization of light and represent a point on the surface of the Poincaré sphere for pure polarization states. In Figure 2, the Bloch sphere is shown on the left, and the Poincaré sphere, with its associated Stokes parameters is shown on the right. The main polarization states discussed so far are illustrated in orange. One can observe that the Stokes-space representation is essentially a rotated version of the Bloch sphere. This highlights one of the advantages of using the Bloch sphere to represent qubits. It can be easily converted into the Stokes-space representation, which is widely used in optics.

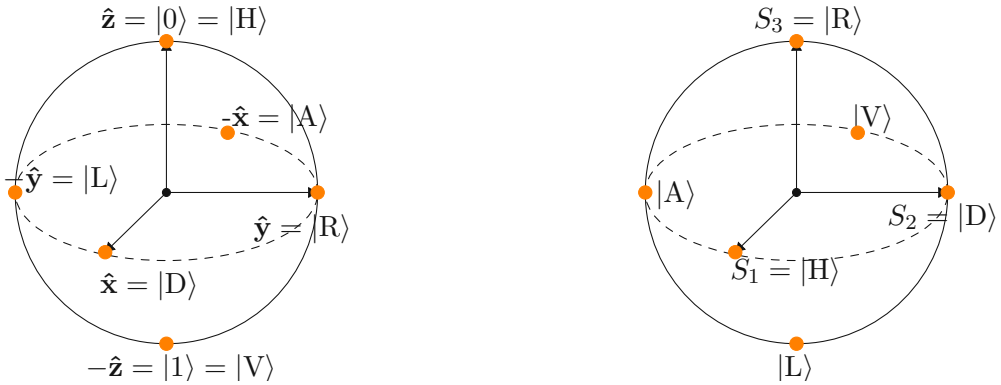

Figure 2: Left: Bloch sphere representation of qubit pure states. Right: Poincaré sphere representation of the corresponding polarization state, expressed via the Stokes vector $\mathbf{S} = (S_1, S_2, S_3)$. The two representations are related by a rotation, highlighting the close connection between qubit states in quantum information and polarization states in optics.

A complete overview of all polarization states presented in this chapter is provided at the end of this chapter in Table 2, expressed in Dirac, Jones, and Stokes notation. While a single qubit already extended the information structure, the real power of quantum communication lies in the correlation between multiple qubits.

2.2 Quantum Entanglement

Quantum entanglement is a phenomenon where two or more qubits become deeply interconnected despite their physical distance [26]. This connection cannot be described by the state of each qubit independently, contrary to classical systems, in which the state of a system can be fully determined by the states of each individual system element. As a result of this connection, the statistical outcome of a measurement is influenced by other qubits. This means when a measurement is performed on one qubit, it instantaneously influences the measurement statistics of the other qubit [27].

Two-Qubit States

The focus of this work is the entanglement between two qubits, each represented by a polarization-encoded photon. So far, only the polarization of a single photon has been considered as the implementation of a qubit. The quantum state of a two-qubit system also exists in a Hilbert space $\mathcal{H}$, defined as the tensor product of the individual qubit Hilbert spaces $\mathcal{H}_1$ and $\mathcal{H}_2$:

$$\mathcal{H} = \mathcal{H}_1 \otimes \mathcal{H}_2.$$

As previously introduced, each qubit is represented by a two-dimensional basis, e.g., $\{|\mathrm{H}\rangle, |\mathrm{V}\rangle\}$, then the combined basis of the two-qubit system is also formed by the tensor products of the individual basis vectors. For instance:

$$|\mathrm{HH}\rangle = |\mathrm{H}\rangle \otimes |\mathrm{H}\rangle = \begin{bmatrix}1\\0\end{bmatrix} \otimes \begin{bmatrix}1\\0\end{bmatrix} = \begin{bmatrix}1\\0\\0\\0\end{bmatrix}, \qquad |\mathrm{HV}\rangle = |\mathrm{H}\rangle \otimes |\mathrm{V}\rangle = \begin{bmatrix}1\\0\end{bmatrix} \otimes \begin{bmatrix}0\\1\end{bmatrix} = \begin{bmatrix}0\\1\\0\\0\end{bmatrix},$$

$$|\mathrm{VH}\rangle = |\mathrm{V}\rangle \otimes |\mathrm{H}\rangle = \begin{bmatrix}0\\1\end{bmatrix} \otimes \begin{bmatrix}1\\0\end{bmatrix} = \begin{bmatrix}0\\0\\1\\0\end{bmatrix}, \qquad |\mathrm{VV}\rangle = |\mathrm{V}\rangle \otimes |\mathrm{V}\rangle = \begin{bmatrix}0\\1\end{bmatrix} \otimes \begin{bmatrix}0\\1\end{bmatrix} = \begin{bmatrix}0\\0\\0\\1\end{bmatrix}.$$

It is important to emphasize that this four-dimensional state vector should not be confused with the Stokes vector. Although both are four-dimensional vectors, because the tensor product of two Jones vectors yields a four-dimensional vector, they have fundamentally different physical meanings.

The individual basis states for the two-qubit system are defined, allowing the general pure two-qubit state in this basis to be written as:

$$|\psi\rangle = a_{\mathrm{HH}}|\mathrm{HH}\rangle + a_{\mathrm{HV}}|\mathrm{HV}\rangle + a_{\mathrm{VH}}|\mathrm{VH}\rangle + a_{\mathrm{VV}}|\mathrm{VV}\rangle,$$

with $|a_{\mathrm{HH}}|^2 + |a_{\mathrm{HV}}|^2 + |a_{\mathrm{VH}}|^2 + |a_{\mathrm{VV}}|^2 = 1$, where $a_{ij} \in \mathbb{C}$ represent the complex amplitudes of the computational two-qubit basis states, respectively.

If the state $|\psi\rangle$ can be factorized into a product of single-photon states, the system is non-entangled. For example:

$$|\psi\rangle = |\psi_1\rangle \otimes |\psi_2\rangle.$$

If no such decomposition exists, the state is entangled. An example of a polarization-entangled state is:

$$|\psi\rangle = \frac{1}{\sqrt{2}}(|\mathrm{HV}\rangle + |\mathrm{VH}\rangle).$$

This state cannot be written as a product of individual qubit states. Physically, this means that if one photon is measured in the horizontal state, the second one must be in the vertical state. This correlation property holds regardless of the spatial separation between them. Nor can this correlation be explained by any local hidden variable model [28]. This concept will be discussed further in section 2.4. An important class of entangled two-qubit states is the set of Bell states, which represent maximally entangled states and form a complete orthonormal basis for the two-qubit Hilbert space.

Nonlinear Polarization and Photon Pair Generation

Polarization-entangled photon pairs can be generated through nonlinear optical processes that conserve both energy and momentum [29]. Spontaneous parametric down-conversion (SPDC) [30] and spontaneous four-wave mixing (SFWM) [31] are two prominent nonlinear processes used to generate entangled photon pairs. Quantum dots [32] can also serve as sources of entangled photons, but they are not explored further in this work.

Nonlinear optical processes arise from the modification of the properties of a material due to the presence of light. In this context, the polarization of a material depends on the strength of the applied optical field. For linear interactions, the polarization is related to the electric field $\mathbf{E}$ through the linear susceptibility $\chi^{(1)}$, as described by the relation:

$$\mathbf{P}_{\text{linear}} = \epsilon_0 \chi^{(1)} \mathbf{E}.$$

Here, ϵ_0 denotes the permittivity of free space. In nonlinear optics, this relation is extended by including higher-order nonlinear susceptibilities such as $\chi^{(2)}$ and $\chi^{(3)}$. Therefore, the susceptibility becomes a function of the electric field, expressed as:

$$\chi(\mathbf{E}) = \chi^{(1)} + \chi^{(2)}\mathbf{E} + \chi^{(3)}\mathbf{E}\mathbf{E} + ...$$

As a result, the total polarization is given by the sum of contributions from different orders:

$$\mathbf{P} = \sum_i \mathbf{P}^{(i)} = \epsilon_0 \chi^{(1)}\mathbf{E} + \epsilon_0 \chi^{(2)}\mathbf{E}\mathbf{E} + \epsilon_0 \chi^{(3)}\mathbf{E}\mathbf{E}\mathbf{E} + ...$$

This allows for a distinction between the linear and nonlinear components of the polarization:

$$\mathbf{P} = \mathbf{P}_{\text{linear}} + \mathbf{P}_{\text{nonlinear}}.$$

Nonlinear polarization is the core concept, which enables SPDC and SFWM. Both processes exploit the nonlinear polarization response of a medium but differ in the order of nonlinearity involved.

SPDC is a second-order nonlinear optical process, which typically occurs in a birefringent crystal. A high-energy pump photon spontaneously splits into two photons on a lower energy level by propagating through a nonlinear crystal, illustrated in Figure 3. These two photons are called signal and idler photons. Depending on the configuration of the crystal, the generated photons can have either orthogonal or the same polarization state. The birefringent crystal is necessary because it enables the phase matching conditions required for this nonlinear conversion.

SFWM is a third-order nonlinear optical process. It involves a pump and a coupling laser and emits a correlated signal idler photon pair, displayed in Figure 3. This process allows the generation of photon pairs with either different frequencies (non-degenerate) or identical frequencies (degenerate), depending on the phase-matching conditions and the experimental setup. An example of non-degenerated SFWM can be found in section 3.1, which discusses the entanglement source used for the experiments carried out in this work.

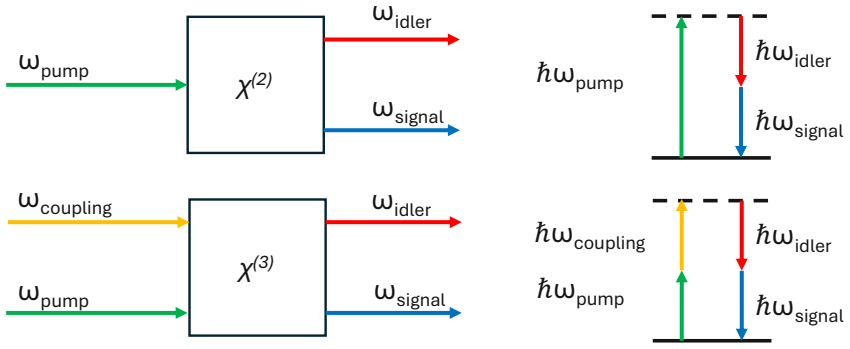

Figure 3: Simplified representation of the energy conservation diagram in SPDC (top) and SFWM (bottom).

2.3 Bell States

The Bell states, named after the physicist John Stewart Bell, are a set of four maximally entangled quantum states of two qubits. They are defined as:

$$|\Phi^+\rangle = \frac{1}{\sqrt{2}}\left(|\mathrm{HH}\rangle + |\mathrm{VV}\rangle\right),$$

$$|\Phi^-\rangle = \frac{1}{\sqrt{2}}\left(|\mathrm{HH}\rangle - |\mathrm{VV}\rangle\right),$$

$$|\Psi^+\rangle = \frac{1}{\sqrt{2}}\left(|\mathrm{HV}\rangle + |\mathrm{VH}\rangle\right),$$

$$|\Psi^-\rangle = \frac{1}{\sqrt{2}}\left(|\mathrm{HV}\rangle - |\mathrm{VH}\rangle\right).$$

These states are typically used in applications involving quantum entanglement distributions. They represent the simplest examples of entanglement between two particles and serve as the basis for quantum communication protocols, for example, the E91 protocol [33]. Additionally, they are used to verify and quantify the entanglement by violating the bell inequality.

2.4 CHSH Inequality

The *Gedankenexperiment* of Einstein Podolsky and Rosen, better known as the EPR paradox published in the paper "Can Quantum-Mechanical Description of Physical Reality be Considered Complete?" [34], started a lively debate. According to the EPR argument, quantum mechanics appears to violate the principle of locality. Einstein called this phenomenon "spooky action at a distance" [35]. This contradiction raised questions about the existence of a hidden-variable theory that could restore a deterministic framework to quantum physics. In 1964 John Bell formulated the Bell inequality, challenging the idea of hidden variables [28]. Building on Bell's inequality, Bell's theorem later demonstrated that no local hidden variable theory could reproduce all the predictions of quantum mechanics. Building upon this foundation, Clauser, Horne, Shimony, and Holt introduced the CHSH inequality in 1969 [36]. This inequality provides a practical experimental test to verify the violation of the locality principle and definitively rules out hidden-variable theories.

The CHSH inequality is expressed as:

$$S = E(a_1, b_1) - E(a_1, b_2) + E(a_2, b_1) + E(a_2, b_2) \leq 2,$$

where $E(a, b)$ represents the quantum correlations of a pair of photons with angles a and b. Each $E(a, b)$ term is given as:

$$E(a, b) = \frac{C(a, b) - C(a, b_\perp) - C(a_\perp, b) + C(a_\perp, b_\perp)}{C(a, b) + C(a, b_\perp) + C(a_\perp, b) + C(a_\perp, b_\perp)},$$

where $a_\perp$ and $b_\perp$ denote directions orthogonal (rotated by 90°) to a and b, respectively.

Local hidden theories require that this inequality set an upper bound of 2 on the absolute value of the sum of certain correlations. Quantum mechanics predicts that this inequality can be violated, allowing values of S to be greater than 2. Exceeding this classical limit of $S \leq 2$ is an important result in the experimental demonstration of quantum entanglement. A maximum violation, known as the Tsirelson bound [37], takes place when $S = 2\sqrt{2}$ and can be achieved with a maximally entangled Bell state.

Polarization State	Dirac	Jones	Stokes
Horizontal	$\|\mathrm{H}\rangle$	$\begin{bmatrix}1\\0\end{bmatrix}$	$\begin{bmatrix}1\\1\\0\\0\end{bmatrix}$
Vertical	$\|\mathrm{V}\rangle$	$\begin{bmatrix}0\\1\end{bmatrix}$	$\begin{bmatrix}1\\-1\\0\\0\end{bmatrix}$
Diagonal	$\|\mathrm{D}\rangle$	$\frac{1}{\sqrt{2}}\begin{bmatrix}1\\1\end{bmatrix}$	$\begin{bmatrix}1\\0\\1\\0\end{bmatrix}$
Anti-Diagonal	$\|\mathrm{A}\rangle$	$\frac{1}{\sqrt{2}}\begin{bmatrix}1\\-1\end{bmatrix}$	$\begin{bmatrix}1\\0\\-1\\0\end{bmatrix}$
Right Circular	$\|\mathrm{R}\rangle$	$\frac{1}{\sqrt{2}}\begin{bmatrix}1\\i\end{bmatrix}$	$\begin{bmatrix}1\\0\\0\\1\end{bmatrix}$
Left Circular	$\|\mathrm{L}\rangle$	$\frac{1}{\sqrt{2}}\begin{bmatrix}1\\-i\end{bmatrix}$	$\begin{bmatrix}1\\0\\0\\-1\end{bmatrix}$

Table 2: Overview of Polarization States in Dirac notation [19], Jones notation [24], and Stokes notation [25].

3 Experimental Setup Elements

This chapter provides an overview of the devices included in the experimental setup. Structured into seven sections, each section offers a detailed explanation of a specific part of the setup to understand the overall system of the experimental framework. An initial setup is shown in chapter 5, in Figure 17.

The first section introduces the entangled photon source and the generation of photon pairs. The second section describes all components within the Bell Box. The third section focuses on the single-photon detection and timing system. The characterization of the field-deployed fiber network is done in the fourth section, highlighting the distinctions between laboratory conditions and the field-deployed infrastructure. The fifth section provides an overview of the automated polarization compensation system and its operational principles. The sixth section explains the switching system and the dynamic routing of photon paths. The final section offers an overview of the classical light channels deployed for co-propagation.

Each section is designed to provide an understanding of the respective component, ensuring an overview of the experimental setup as a whole.

3.1 Entangled Photon Source

The entanglement source is a key building block of every setup for quantum networking. Specifically in this study, i.e., for distributing polarization-encoded qubits, the setup needs a source which provides the polarization-entangled photon pairs. The source has to satisfy a number of criteria simultaneously, such as high-rate generation, narrow line-width photons, high fidelity, and heralding efficiency. In this work, a commercially available bichromatic entanglement source was used [31].

The source generates entangled photon pairs via SFWM in a process where a warm rubidium (^{87}Rb) vapor cell is pumped by a 780 nm pump laser and a 1367 nm coupling laser. These lasers excite the rubidium atoms from the ground state to a doubly-excited state. The subsequent decay from this state back to the ground state occurs in a phase-matched direction, where the wavevectors $\vec{k}$ satisfy the condition:

$$\vec{k}_{pump} + \vec{k}_{coupling} - \vec{k}_{signal} - \vec{k}_{idler} = 0\,.$$

This process, illustrated in Figure 4, generates strongly correlated signal and idler photon pairs with wavelengths of 1324 nm (signal) and 795 nm (idler). The pump and coupling beams are overlapped by using a dichroic mirror to ensure copropagation, and a polarizing beam splitter guarantees identical polarization before entering the rubidium vapor cell. The beams are coupled into and out of the vapor cell using lenses to ensure phase matching. The cell is heated by a pair of metal-ceramic heaters placed directly on its faces. After

exiting the cell, a dichroic mirror separates the signal and idler beams. Since both the signal and idler photons are emitted with identical polarization, the resulting two-photon state corresponds to the well-known Bell state $|\Phi^+\rangle$, which takes the form:

$$|\Phi^+\rangle = \frac{1}{\sqrt{2}}(|\mathrm{HH}\rangle + e^{i\phi}|\mathrm{VV}\rangle)\,.$$

A liquid crystal retarder is used to overcome phase shifts induced by the internal components of the device.

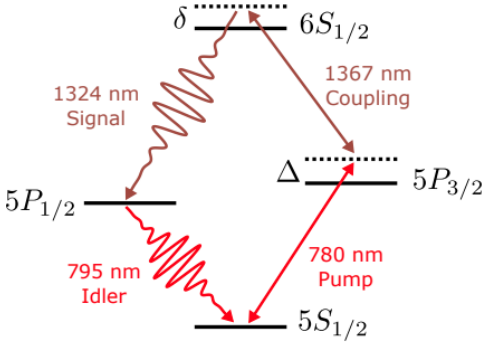

Figure 4: Rubidium level diagram for the four-wave mixing process [31].

3.2 Bell Box

The Bell box represents the initial stage of the measurement process. It performs the first step in characterizing the entangled photon signal. In this section, the individual optical components within the Bell box are described separately to provide a clear understanding of their functions and roles. A detailed characterization of the complete measurement procedure, including the complete mathematical derivation, is provided in chapter 4.

Since the polarization manipulation is performed more precisely in free space, the photons have to leave the guided fibers. For this reason, the Bell box includes a fiber-to-free space coupler and a free-space to fiber interface. This enables free-space transmission to perform measurements with rotating waveplates and a polarized beam splitter.

Waveplates

A waveplate, also known as a retarder, introduces a phase shift between the orthogonal polarization components of an electromagnetic wave. In optical systems, waveplates are essential components for manipulating and analyzing the polarization state of light. Their operation can be accurately described using the Jones notation. Although waveplates can be designed to introduce arbitrary phase delays between polarization components, the half-waveplate (HWP) and the quarter-waveplate (QWP) are the most commonly used in practice. The half-waveplate is also known as the $\lambda/2$-waveplate and the quarter-waveplate is also known as the $\lambda/4$-waveplate. These elements rely on birefringent materials that exhibit different refractive indices. As a result, the waveplate modifies the polarization state of the transmitted light in a predictable and controllable way. Since the Bell box operates with the $\lambda/2$-waveplate, we explore its function in more detail. An HWP introduces a phase shift of π (or 180°) between the fast and slow axes. If the fast axis is aligned horizontally, the Jones matrix of the HWP is given by:

$$\mathbf{J}_{\lambda/2} = \begin{bmatrix} 1 & 0 \\ 0 & -1 \end{bmatrix}.$$

Polarized Beam Splitter

A polarized beam splitter (PBS) is an optical element that separates incoming light on the basis of its polarization. The PBS transmits one polarization state while reflecting the orthogonal component. This results in one part of the light having horizontal polarization and the other part having vertical polarization. The action of a PBS can be represented by using Jones notation. The Jones matrices for the two output paths are written for the transmitted path (T), corresponding to horizontal polarization, and the reflected path (R) corresponding to vertical polarization.

$$\mathbf{J}^{\mathrm{T}}_{\mathrm{PBS}} = \begin{bmatrix} 1 & 0 \\ 0 & 0 \end{bmatrix},$$

$$\mathbf{J}^{\mathrm{R}}_{\mathrm{PBS}} = \begin{bmatrix} 0 & 0 \\ 0 & 1 \end{bmatrix}.$$

If a light beam enters the PBS with an arbitrary polarization state, the PBS will direct the vertical component along the transmitted path and the vertical state along the reflected path.

While a light beam can be described as a continuous wave, when a photon enters the PBS, its individual polarization state is measured, leading to a collapse of the superposition. For example, when a photon in the superposition state, such as $|\mathrm{D}\rangle = \frac{1}{\sqrt{2}}(|\mathrm{H}\rangle + |\mathrm{V}\rangle)$, enters the PBS, the device performs a measurement in the vertical and horizontal basis. When detected in one of the output ports, the state of the photon collapses into the corresponding eigenstate. For instance, if the photon is detected in the transmitted path, the state collapses to $|\mathrm{H}\rangle$. This projection is fundamental in quantum optics. The PBS acts as a measurement device that extracts polarization information from single photon by collapsing the superposition states.

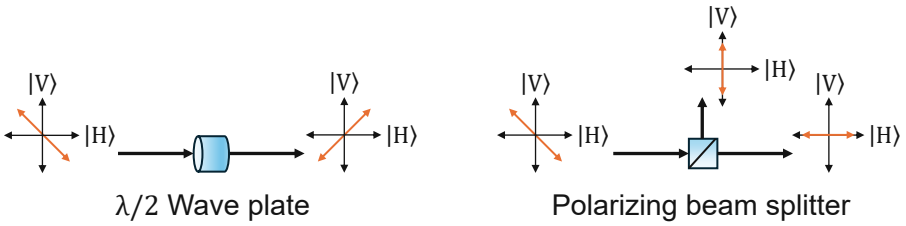

Figure 5: Left: Polarization modification via half-waveplate. Right: Polarization dependent output of a PBS.

3.3 Single Photon Detection

The second and final stage of the measurement process consists of a superconducting nanowire single photon detector [38] and a timing system. This process allows to create time-stamped photons counting within temporal resolution down to picoseconds.

Superconducting Nanowire Single Photon Detector

Single-photon detection relies on converting the energy of an incident photon into a measurable electrical signal. When a photon hits the detector, it is absorbed by the detector material, creating an electrical pulse that can be registered. This process depends on the properties and geometry of the detection material as well as the operating conditions. Superconducting nanowire single-photon detectors (SNSPDs) have excellent detection efficiency, low dark count rates, and fast recovery times.

The basic operation of an SNSPD, from incident photon to electrical pulse, is illustrated in Figure 6. A nanowire is cooled below its superconducting critical temperature, and a direct current is applied. When an incident photon enters the active area of the detector, it is absorbed and breaks Cooper pairs, thereby forming a hotspot. The hotspot region forces the current to flow around the resistive area, causing an increase in current density in the sidewalk regions until it reaches a critical level. This forms a resistive barrier across

the nanowire and generates a measurable voltage pulse as the resistance rises from zero to a finite value. While most of the current does not flow over the nanowire, it cools down and returns to the superconducting state.

The system detection efficiency (SDE) η_{SDE} is defined as:

$$\eta_{\text{SDE}} = \eta_{\text{coupling}}\, \eta_{\text{absorption}}\, \eta_{\text{register}}\,,$$

where the coupling efficiency η_{coupling} addresses factors such as imperfect optics, fiber coupling, and reflections. It describes the losses before the photon reaches the detection material. The absorption efficiency $\eta_{\text{absorption}}$ depends on the material and geometry of the detector. Also changes with the wavelength of the photon. η_{register} defines the registration probability, which characterizes how likely an absorption event triggers a measurable electrical pulse. Sometimes, intrinsic device detection efficiency (DDE) is used η_{DDE}, which excludes the coupling efficiency, $\eta_{\text{DDE}} = \eta_{\text{absorption}}\, \eta_{\text{register}}$.

Further performance parameters are the dark count rate, jitter, and recovery time, which define the practical usability of the detector. The dark count rate refers to counts without incident photons. Jitter is the difference between the actual arrival time of the photon and the generated electrical pulse. It is essential for high temporal resolution and should be as low as possible. Recovery time is the period in which the detector cannot register the next incoming photon after a detection event. The cooling system is a minor drawback, which is typically achieved using liquid helium or cryogenic probes to maintain superconductivity. To deliver photons into the low-temperature environment, an optical coupling window is installed. In contrast, single-photon avalanche photo diodes (SPADs) operate at or near room temperature, but they have higher dark-count rates and jitter.

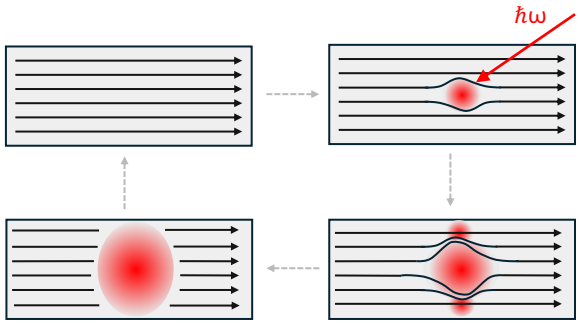

Figure 6: Basic operation principle of SNSPD. Top Left: In the steady state, the nanowire is fully superconducting, and electric current flows through it. Top Right: An incoming photon strikes the nanowire, its energy is absorbed, disrupting the local superconducting state. Bottom Right: The absorbed energy creates a small hotspot, which heats up as the current is forced to divert around it. Bottom Left: The hotspot acts as a barrier, temporarily breaking the superconducting path and generating a measurable voltage pulse.

Time Tagger

A time tagger is a device that generates precise timestamps for the arrival of incoming pulses, such as those created by an SNSPD. The signal and idler photons are detected on different channels, each producing its own time series $t_{\mathrm{CH1}}[n]$ and $t_{\mathrm{CH2}}[m]$, respectively. A histogram of the time differences Δt between events on the two channels is constructed by performing a cross-correlation to generate coincidence peaks.

Since entangled photon pairs are created at the same time and the path delay remains constant, a coincidence peak appears at a specific time offset in the histogram. The coincidence peak marks the relative travel time between the two optical paths. If the idler photons remain local and the signal photons travel a longer path, the peak appears at a non-zero time delay corresponding to the path difference. For improving the visibility of the coincidence peak, it is possible to increase the integration times, to detect more incoming photons. This is important for longer or more lossy optical paths, although it comes with the drawback of extended data acquisition periods.

In addition to the coincidence peak, a noise floor arises due to accidental coincidence, which are random detection events that fall within the coincidence window but do not originate from entangled pairs. Factors such as detector jitter, time tagger jitter, and bin width affect the sharpness of the peak.

3.4 Field Deployed Fiber

To address key differences between field-deployed fiber and controlled laboratory conditions, optical time-domain measurements were conducted on the field-deployed dark fiber network at T-Labs in Berlin, shown in Figure 7. Unlike laboratory setups, deployed fiber introduces several challenges, particularly for polarization-entangled photons, which are highly sensitive to environmental disturbances [39]. Stochastic fluctuations in polarization

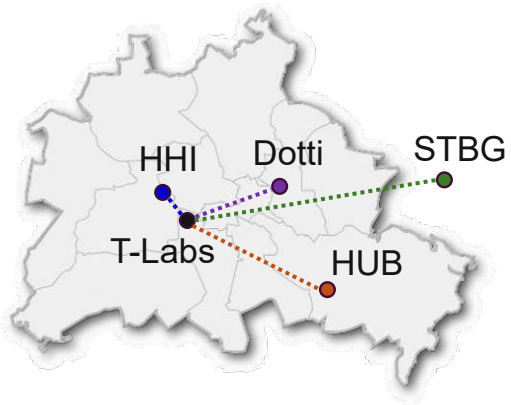

Figure 7: Geographical distribution of studied fiber loops terminated at T-Labs in Berlin (HHI: Heinrich-Hertz-Institut, Dotti: Dottistraße, STBG: Strausberg, HUB: Humboldt University - Department of Physics).

arise from changes in the refractive index and physical length. These changes are caused by factors such as temperature variations, mechanical stress, pressure, and bending. As a result, the polarization state of optical signals shifts in an unpredictable way over time [40].

OTDR Measurements

An optical time domain measurement works on the same principle as electrical time domain reflectometry. A laser pulse is sent through an optical fiber. As the pulse travels along the fiber, imperfections, such as connectors, splices, and other forms of attenuation, cause parts of the pulse to reflect back. The measurement creates a signal profile, known as the trace, based on two main aspects. First, the time of flight determines how long the pulse has traveled, allowing the distance to each reflecting point to be calculated. Second, the back scattered light provides information about the overall attenuation along the fiber.

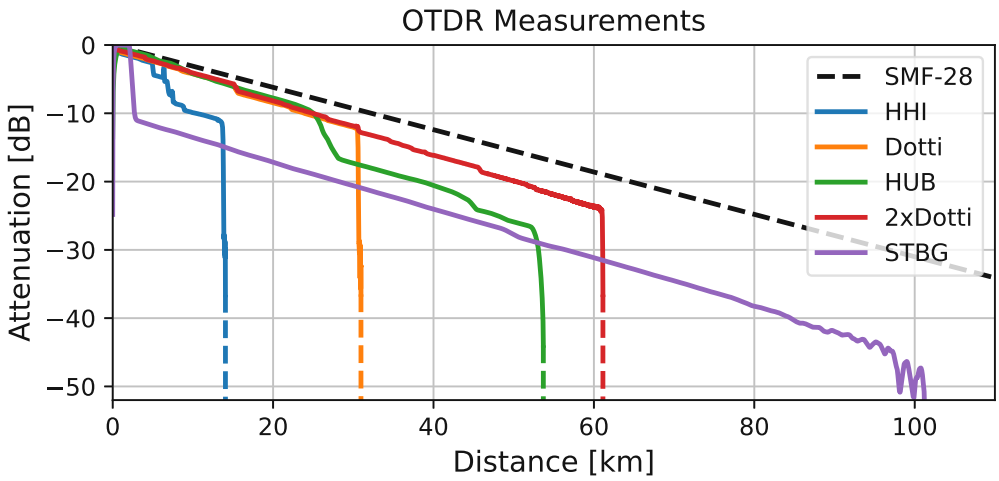

Figure 8: OTDR measurements of field-deployed fibers used individually or stitched together. For reference, the attenuation of standard SMF-28 single-mode fiber at 1310 nm. 2xDotti represent two distinct fiber loops connected locally in the lab, both run via Dottistraße.

Measurements were carried out and the results for ∼ 15 km Heinrich-Hertz-Institut (HHI), ∼ 30 km Dottistraße (Dotti), ∼ 50 km Humboldt University (HUB), ∼ 60 km two fiber loops via Dottistraße (2× Dotti), or ∼ 100 km Strausberg (STBG) (specifically: 13.6, 30.5, 51.8 61.0 and 97.9 km) are shown in Figure 8. A reference trace of an ideal single mode fiber at 1310 nm is also included, showing a best-case scenario for comparison.

3.5 Automated Polarization Compensation

Transmission of polarization-encoded photons is very complex due to polarization shifts and drifts caused by environmental factors, as discovered in previous sections. These changes in the polarization state can impair the distribution of entanglement. Therefore, an automatic polarization control system (APC) is essential to counteract these stochastic effects [15].

The APC system, illustrated in Figure 9, consists of two parts, an injector and a compensator. Inside the injector, an optical switch selects between the quantum signal input and a classical laser light input. This classical probe light is generated within the device and serves as a reference frame for the compensation. Six distinct points on the Poincaré sphere are used as a reference. After transmission through the fiber, the probe is affected by the channel and appears at different positions on the Poincaré sphere. The second part of the system, the compensator, tries to return these points to their original positions using a polarization controller. Within a feedback loop, the compensator evaluates a classical fidelity based on the reference frame and tries to reach a predefined target threshold. Once this threshold is achieved, the quantum signal transmission is resumed.

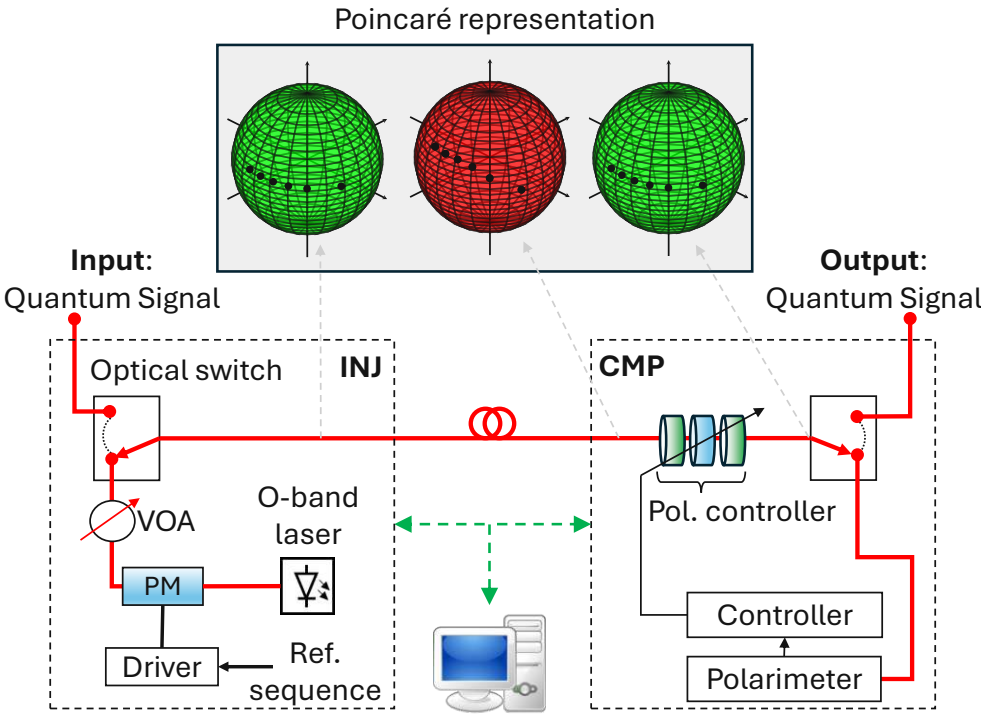

Figure 9: Relevant representation of the APC System, including the injector (INJ) and compensator (CMP). The Poincaré representation illustrates the polarization states at different stages of the transmission. Green: Reference (left) and reconstructed (right) points. Red (middle): Polarization drift caused by the fiber. (VOA: variable optical attenuator, PM: polarization modulator)

The system operates in a time-multiplexed scheme to compensate for polarization drift

at a specific wavelength. Since polarization drift is wavelength dependent [39], the system performs best when the classical probe light and the quantum signal share the same wavelength.

3.6 Optical Switching System

A mechanical optical cross switch 2x2 is used to change the direction of the distributed quantum signal, across different paths. The switch operates in two modes, cross and bypass mode and is triggered via a serial connection. In bypass mode, the switch directs the input signal from port 1 to port 2 and the input signal from port 4 to port 3, while in cross mode, the input signal from port 1 is routed to port 3, and from port 4 to port 2.

In the experiments, the switch was used to create distribution over different paths. By using port 1 as the input port for the quantum signal and port 2 as the output, back to the measurement station, a local path is created in bypass mode. When switched to cross mode, the input from port 1 is redirected to port 3, which is connected to the field-deployed fiber, then returns to input port 4, which is connected with port 2. These variants are exactly illustrated in Figure 10.

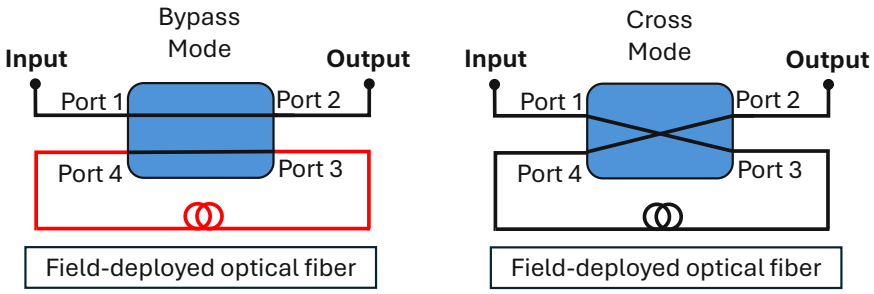

Figure 10: Left: The optical switch in bypass mode establishes a local path within the lab. Right: Cross mode uses the field-deployed fiber path.

For distribution via two different field-deployed paths, the switch is used with three ports. Input port 1 switches between port 2 or port 3, which are connected to two different field-deployed fibers. The paths are then combined after transmission using a beam splitter.

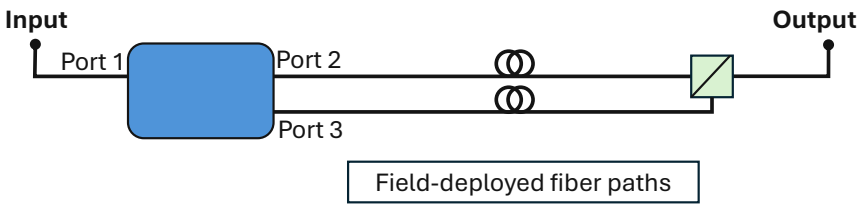

Figure 11: An optical switch selects between two different fiber paths, which are then combined in the lab using a beam splitter.

3.7 Classical Light Channel

To emulate a classical light signal, two different generation approaches were implemented. In the first method, noise shaping was carried out using a C-band erbium-doped fiber amplifier (EDFA) setup. Without an input signal, the EDFA generates amplified spontaneous emission (ASE) noise, which was shaped into a 50 GHz wide channel using a programmable optical filter. The filtered noise was then amplified again using a second EDFA to increase the optical power and flexibility, shown in the spectra plots of Figure 12.

In the second approach, a 50 GHz dense wavelength division multiplexing (DWDM) channel was employed. The optical signal was amplified with an EDFA, and a programmable optical filter was used to suppress the ASE noise floor produced by the EDFA. This method allows more precise control over the spectral properties of the classical signal.

In both cases, the resulting classical light was then multiplexed into the same fiber as the quantum signal using an optical add-drop multiplexer (OADM). This configuration enables the simultaneous transmission of classical and quantum signal over a shared fiber. Prior to detection, the quantum signal was separated from the classical channel using a second OADM. The quantum path was additionally filtered within the Bell box to reduce noise inference at the SNSPD.

These approaches enable controlled emulation of the copropagation from classical and quantum signals to evaluate the performance of distributing entangled photons under realistic network conditions.

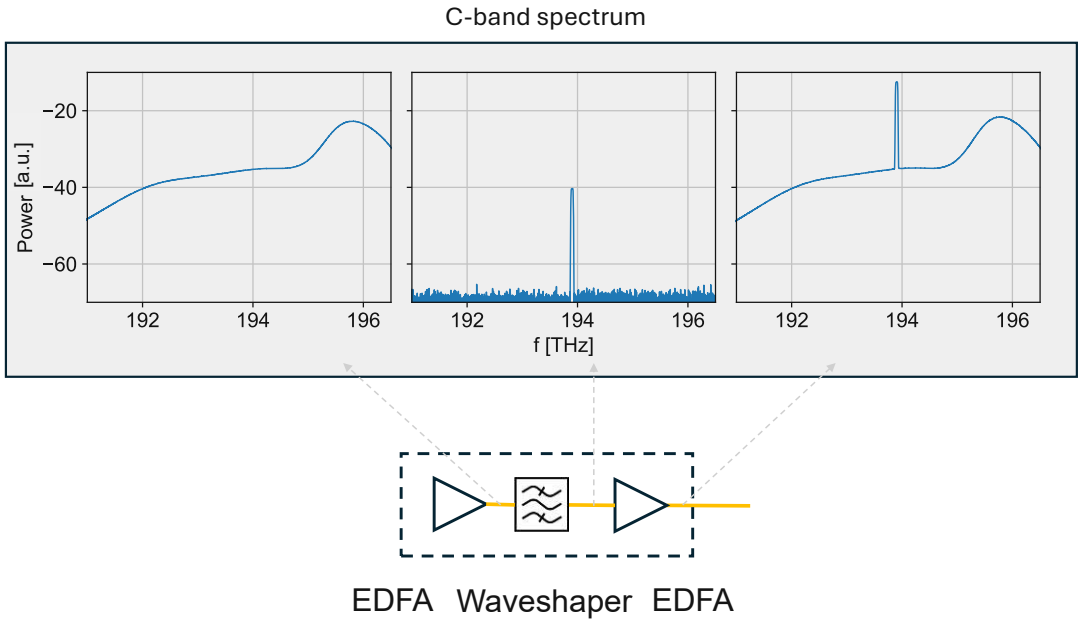

Figure 12: Left: Spectrum of the ASE. Middle: Shaped noise spectrum. Right: Amplified shaped noise spectrum.

4 Methodology

This chapter provides the basis for the analysis carried out in the experiments. In the first section, a detailed derivation of the CHSH test is done, including the experimental components. The second section explains how data processing generates reliable results. To proceed with both sections, it is important to be aware of the exact measurement setup, see Figure 13.

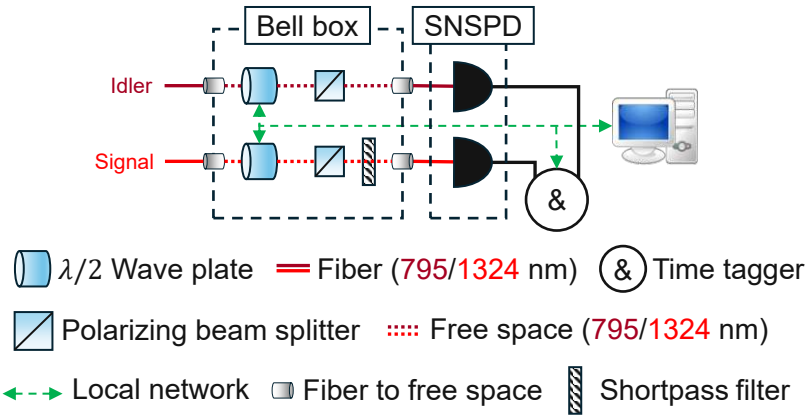

Figure 13: A detailed view of the measurement station, showing incoming signal and idler photons.

4.1 Derivation for CHSH Test

Since the CHSH test is not intuitive to understand, a detailed mathematical derivation is provided, using the components introduced in chapter 3. The preparation for the measurement is done in the Bell box. The Bell box includes an experimental configuration with a motorized rotating $\lambda/2$-waveplate and a polarized beam splitter.

Modeling Polarization Rotation

The Jones matrix representation for a rotating $\lambda/2$-waveplate depends on how the plate is oriented within the optical system and affects the polarization state of light during rotation. As already shown, the Jones transfer matrix for a $\lambda/2$-waveplate is:

$$\mathbf{J}_{\lambda/2} = \begin{bmatrix} 1 & 0 \\ 0 & -1 \end{bmatrix}.$$

This matrix applies a phase shift between the two orthogonal polarization components. When the plate rotates, the Jones notation must take into account the orientation of the plate relative to the polarization direction of the light. The rotation of the plate changes the effect of the waveplate. This change is mathematically formulated using a rotation matrix, which shifts the coordinate system of the Jones matrix. The rotation matrix is defined as:

$$\mathbf{R}(\theta) = \begin{bmatrix} \cos\theta & \sin\theta \\ -\sin\theta & \cos\theta \end{bmatrix}.$$

The complete transmission matrix for a rotated $\lambda/2$-waveplate is obtained by combining the rotation matrix and the $\lambda/2$-waveplate as follows:

$$\mathbf{J}_{\lambda/2}(\theta) = \mathbf{R}^{-1}(\theta)\,\mathbf{J}_{\lambda/2}\,\mathbf{R}(\theta)\,.$$

Since the rotation matrix is orthogonal, it follows that $\mathbf{R}^{-1}(\theta) = \mathbf{R}(-\theta)$ and results in:

$$\mathbf{J}_{\lambda/2}(\theta) = \begin{bmatrix} \cos\theta & -\sin\theta \\ \sin\theta & \cos\theta \end{bmatrix} \begin{bmatrix} 1 & 0 \\ 0 & -1 \end{bmatrix} \begin{bmatrix} \cos\theta & \sin\theta \\ -\sin\theta & \cos\theta \end{bmatrix}$$

$$= \begin{bmatrix} \cos\theta & -\sin\theta \\ \sin\theta & \cos\theta \end{bmatrix} \begin{bmatrix} \cos\theta & \sin\theta \\ \sin\theta & -\cos\theta \end{bmatrix} = \begin{bmatrix} \cos^2\theta - \sin^2\theta & \cos\theta\sin\theta + \sin\theta\cos\theta \\ \sin\theta\cos\theta + \cos\theta\sin\theta & \sin^2\theta - \cos^2\theta \end{bmatrix}.$$

Using the double angle identity $\cos(2\theta) = \cos^2(\theta) - \sin^2(\theta)$ and $\sin(2\theta) = 2\sin(\theta)\cos(\theta)$, the Jones transfer matrix is simplified to:

$$\mathbf{J}_{\lambda/2}(\theta) = \begin{bmatrix} \cos(2\theta) & \sin(2\theta) \\ \sin(2\theta) & -\cos(2\theta) \end{bmatrix}.$$

In the next step, a polarizing beam splitter is introduced. When horizontally polarized photons $|\mathrm{H}\rangle$ pass through the rotating half-waveplate, following result is obtained at the transmitting output of the PBS:

$$|\psi_{out}\rangle = \mathbf{J}^{\mathrm{T}}_{\mathrm{PBS}}\mathbf{J}_{\lambda/2}(\theta)|\mathrm{H}\rangle$$

$$= \begin{bmatrix} 1 & 0 \\ 0 & 0 \end{bmatrix} \begin{bmatrix} \cos(2\theta) & \sin(2\theta) \\ \sin(2\theta) & -\cos(2\theta) \end{bmatrix} \begin{bmatrix} 1 \\ 0 \end{bmatrix} = \begin{bmatrix} 1 & 0 \\ 0 & 0 \end{bmatrix} \begin{bmatrix} \cos(2\theta) \\ \sin(2\theta) \end{bmatrix}$$

$$|\psi_{out}\rangle = \begin{bmatrix} \cos(2\theta) \\ 0 \end{bmatrix}.$$

To detect a single photon, the detection probability of the output state $|\psi_{out}\rangle$ is given by the square of the qubit's amplitude:

$$P = ||\psi_{\mathrm{out}}\rangle|^2 = |\cos(2\theta)|^2 = \cos^2(2\theta)\,.$$

This result shows that the detection probability depends on the angle 2θ, where θ is the angle between the input polarization direction and the optical axis of the half-waveplate. The

PBS then transmits only the horizontal component of the modified polarization, resulting in a cosine-squared dependence. Note that this setup, where a rotating half-waveplate is in front of a fixed PBS, is functionally different from rotating the PBS itself.

Correlation Functions in Two-Qubit Systems

A general observable $\hat{\sigma}_{\theta,\phi}$ can be expressed as a linear combination of the Pauli operators:

$$\hat{\sigma}_{\theta,\phi} = \sin(\theta)\cos(\phi)\hat{\sigma}_x + \sin(\theta)\sin(\phi)\hat{\sigma}_y + \cos(\theta)\hat{\sigma}_z \,.$$

The corresponding Pauli spin matrices are given by:

$$\hat{\sigma}_x = \begin{bmatrix} 0 & 1 \\ 1 & 0 \end{bmatrix}, \quad \hat{\sigma}_y = \begin{bmatrix} 0 & -i \\ i & 0 \end{bmatrix}, \quad \hat{\sigma}_z = \begin{bmatrix} 1 & 0 \\ 0 & -1 \end{bmatrix}.$$

Assuming the rotation of the linearly polarized state is restricted to the x-z plane, this implies that $\phi = 0$. With this condition, the observable is given by:

$$\hat{\sigma}_{\theta,0} = \cos(\theta)\hat{\sigma}_z + \sin(\theta)\hat{\sigma}_x = \begin{bmatrix} \cos(\theta) & \sin(\theta) \\ \sin(\theta) & -\cos(\theta) \end{bmatrix}.$$

The quantum mechanical correlation function of the measurement outcomes for two qubits, as a function of the angles α and β, is given by:

$$E_{QM}(\alpha,\beta) = \langle \Phi^+ | \, \hat{\sigma}_{\alpha,0} \otimes \hat{\sigma}_{\beta,0} \, | \Phi^+ \rangle \,.$$

The Bell state $|\Phi^+\rangle$ is given in Jones vector notation as:

$$|\Phi^+\rangle = \frac{1}{\sqrt{2}}(|\mathrm{HH}\rangle + |\mathrm{VV}\rangle) = \frac{1}{\sqrt{2}} \begin{bmatrix} 1 \\ 0 \\ 0 \\ 1 \end{bmatrix}.$$

Definition of the measurement operator for a two-qubit system, based on two different measurement angles α and β, is written as:

$$\hat{A} \coloneqq \hat{\sigma}_{\alpha,0} \otimes \hat{\sigma}_{\beta,0}$$

$$= \begin{bmatrix} \cos(\alpha) & \sin(\alpha) \\ \sin(\alpha) & -\cos(\alpha) \end{bmatrix} \otimes \begin{bmatrix} \cos(\beta) & \sin(\beta) \\ \sin(\beta) & -\cos(\beta) \end{bmatrix}$$

$$= \begin{bmatrix} \cos(\alpha)\cos(\beta) & \cos(\alpha)\sin(\beta) & \sin(\alpha)\cos(\beta) & \sin(\alpha)\sin(\beta) \\ \cos(\alpha)\sin(\beta) & -\cos(\alpha)\cos(\beta) & \sin(\alpha)\sin(\beta) & -\sin(\alpha)\cos(\beta) \\ \sin(\alpha)\cos(\beta) & \sin(\alpha)\sin(\beta) & -\cos(\alpha)\cos(\beta) & -\cos(\alpha)\sin(\beta) \\ \sin(\alpha)\sin(\beta) & -\sin(\alpha)\cos(\beta) & -\cos(\alpha)\sin(\beta) & \cos(\alpha)\cos(\beta) \end{bmatrix}.$$

All the components can be substituted into the quantum mechanical correlation function:

$$E_{QM}(\alpha,\beta) = \langle \Phi^+ | \, \hat{A} \, | \Phi^+ \rangle$$

$$= \frac{1}{\sqrt{2}} \begin{bmatrix} 1 & 0 & 0 & 1 \end{bmatrix} \begin{bmatrix} \cos(\alpha)\cos(\beta) & \cos(\alpha)\sin(\beta) & \sin(\alpha)\cos(\beta) & \sin(\alpha)\sin(\beta) \\ \cos(\alpha)\sin(\beta) & -\cos(\alpha)\cos(\beta) & \sin(\alpha)\sin(\beta) & -\sin(\alpha)\cos(\beta) \\ \sin(\alpha)\cos(\beta) & \sin(\alpha)\sin(\beta) & -\cos(\alpha)\cos(\beta) & -\cos(\alpha)\sin(\beta) \\ \sin(\alpha)\sin(\beta) & -\sin(\alpha)\cos(\beta) & -\cos(\alpha)\sin(\beta) & \cos(\alpha)\cos(\beta) \end{bmatrix} \frac{1}{\sqrt{2}} \begin{bmatrix} 1 \\ 0 \\ 0 \\ 1 \end{bmatrix}$$

$$= \frac{1}{2}(\cos(\alpha)\cos(\beta) + \sin(\alpha)\sin(\beta) + \sin(\alpha)\sin(\beta) + \cos(\alpha)\cos(\beta)) \, .$$

Using the cosine addition formula $\cos(\alpha)\cos(\beta) + \sin(\alpha)\sin(\beta) = \cos(\alpha - \beta)$ the final result assumes the following expression:

$$E_{QM}(\alpha,\beta) = \cos(\alpha - \beta) \, .$$

Maximal Quantum Violation of CHSH Inequality

To demonstrate the maximal violation of the inequality, the following angles are used:

$$\alpha_1 = 0, \quad \alpha_2 = \frac{\pi}{4}, \quad \beta_1 = \frac{\pi}{8}, \quad \beta_2 = \frac{3\pi}{8}.$$

Since photons repeat their polarization with a period of π, the correlations depend on twice the angle difference, resulting in the correlation function:

$$E(\alpha,\beta) = \cos\big(2(\alpha - \beta)\big) \, .$$

Correlation values, respectively:

$$E(\alpha_1,\beta_1) = \cos\big(2(0 - \frac{\pi}{8})\big) = \cos\left(-\frac{\pi}{4}\right) = \frac{\sqrt{2}}{2},$$
$$E(\alpha_1,\beta_2) = \cos\big(2(0 - \frac{3\pi}{8})\big) = \cos\left(-\frac{3\pi}{4}\right) = -\frac{\sqrt{2}}{2},$$
$$E(\alpha_2,\beta_1) = \cos\big(2(\frac{\pi}{4} - \frac{\pi}{8})\big) = \cos\left(\frac{\pi}{4}\right) = \frac{\sqrt{2}}{2},$$
$$E(\alpha_2,\beta_2) = \cos\big(2(\frac{\pi}{4} - \frac{3\pi}{8})\big) = \cos\left(-\frac{\pi}{4}\right) = \frac{\sqrt{2}}{2}.$$

The Bell parameter S was then calculated as:

$$S = E(\alpha_1,\beta_1) - E(\alpha_1,\beta_2) + E(\alpha_2,\beta_1) + E(\alpha_2,\beta_2)$$
$$= \frac{\sqrt{2}}{2} + \frac{\sqrt{2}}{2} + \frac{\sqrt{2}}{2} + \frac{\sqrt{2}}{2} = 2\sqrt{2} \approx 2.828 \, .$$

This represents the maximum quantum violation of the Bell inequality, reaching the Tsirelson bound [37] of $S = 2\sqrt{2}$.

4.2 Data Processing

This section gives a detailed description of the processing steps applied to the raw measurement data. This procedure is used for all experiments and evaluations. All results presented later in this work are based on this approach. The detailed analysis outlines the extraction of the coincidence peak, construction of the Bell parameter and fidelity, and statistical error estimation. The Bell parameter (S-value) quantifies nonlocal correlations, while the fidelity serves as a measure of the closeness between the measured and transmitted quantum states.

Bell Parameter

The raw measurement data consist of time-tagged photon detection events, with varying angle settings prepared within the Bell box. The total estimation set includes 4 distinct angles for the idler waveplate, each paired with 17 unique angles for the signal waveplate. A total of 68 unique angle measurement combinations. Each subplot represents the corresponding coincidence counts, according to an individual angle combination. The subplots are organized into four columns in different colors, with the same idler waveplate setting. The rows always have the same signal waveplate setting. To acquire a complete data set, the idler waveplate is set to $0°, 22.5°, 45°$, and $67.5°$ and the signal waveplate is adjusted in $11.5°$ steps covering the range from $0°$ to $180°$.

For each pair of angles, the maximal coincidence count is extracted, representing the number of detection events registered simultaneously on two detectors. This peak corresponds to photons from the same entangled pair. The coincidence peak is identified within a specific time window, determined by the path length traveled by the photons.

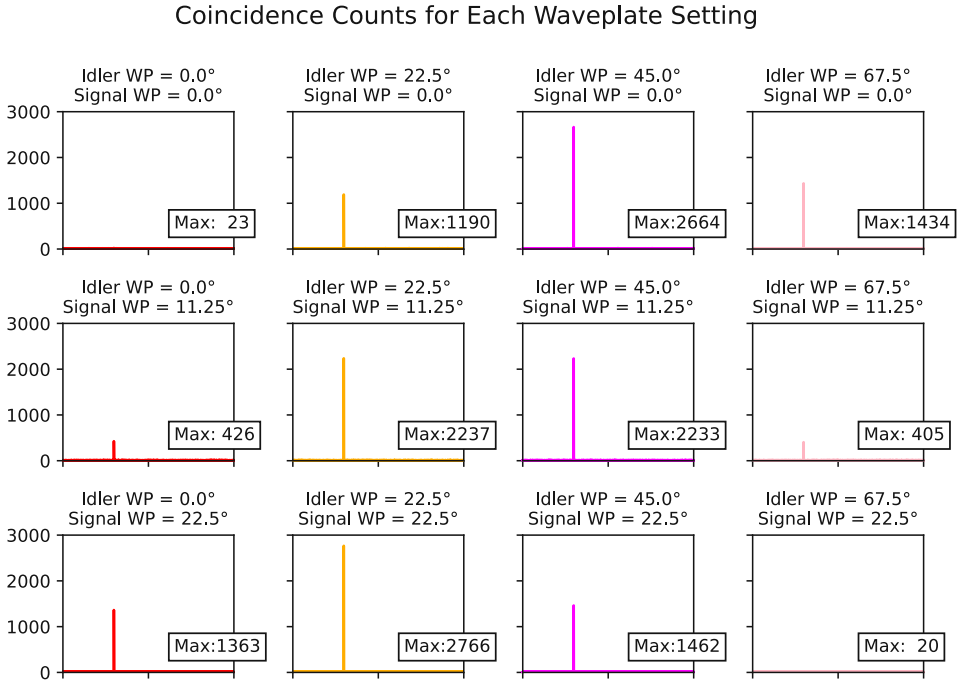

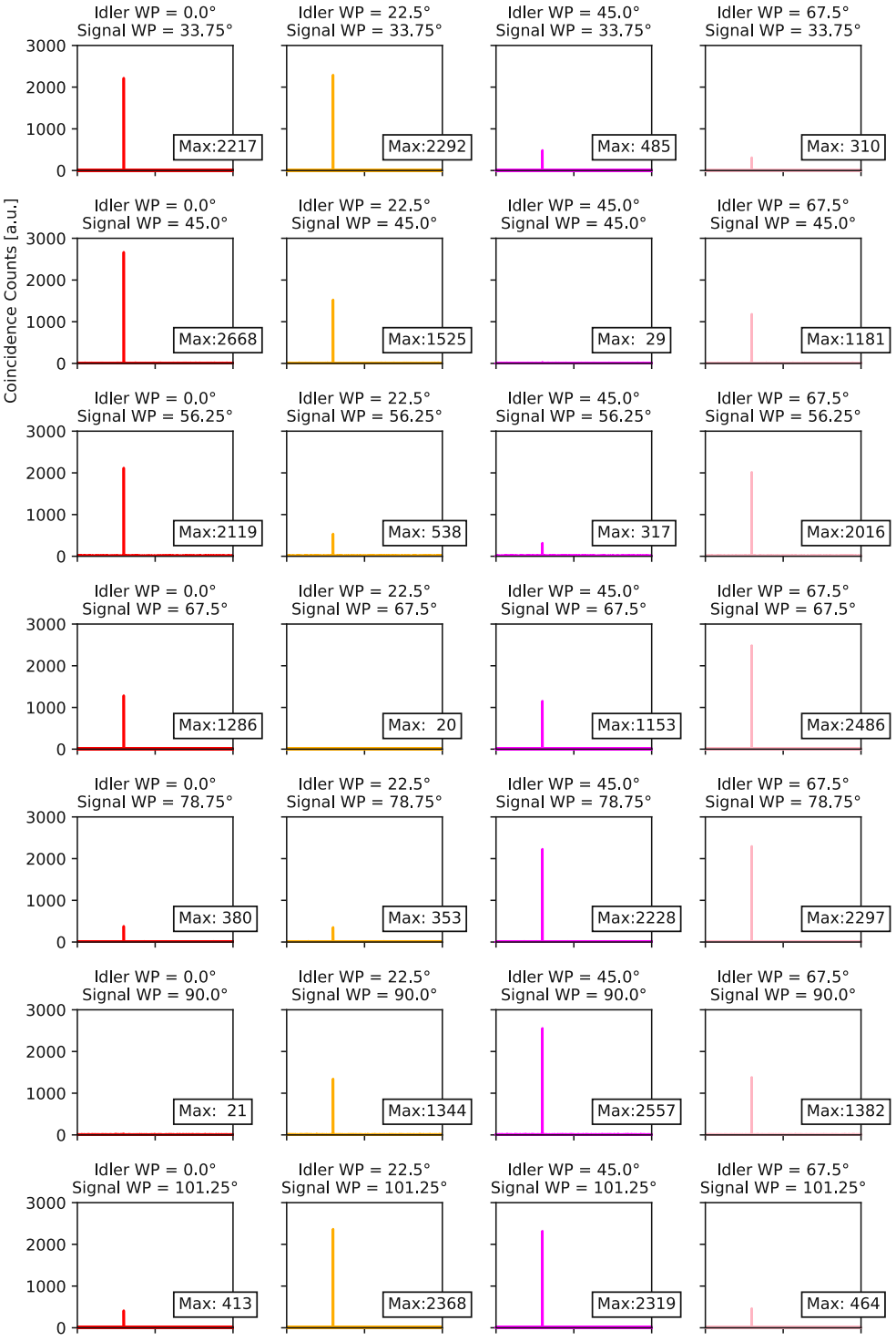

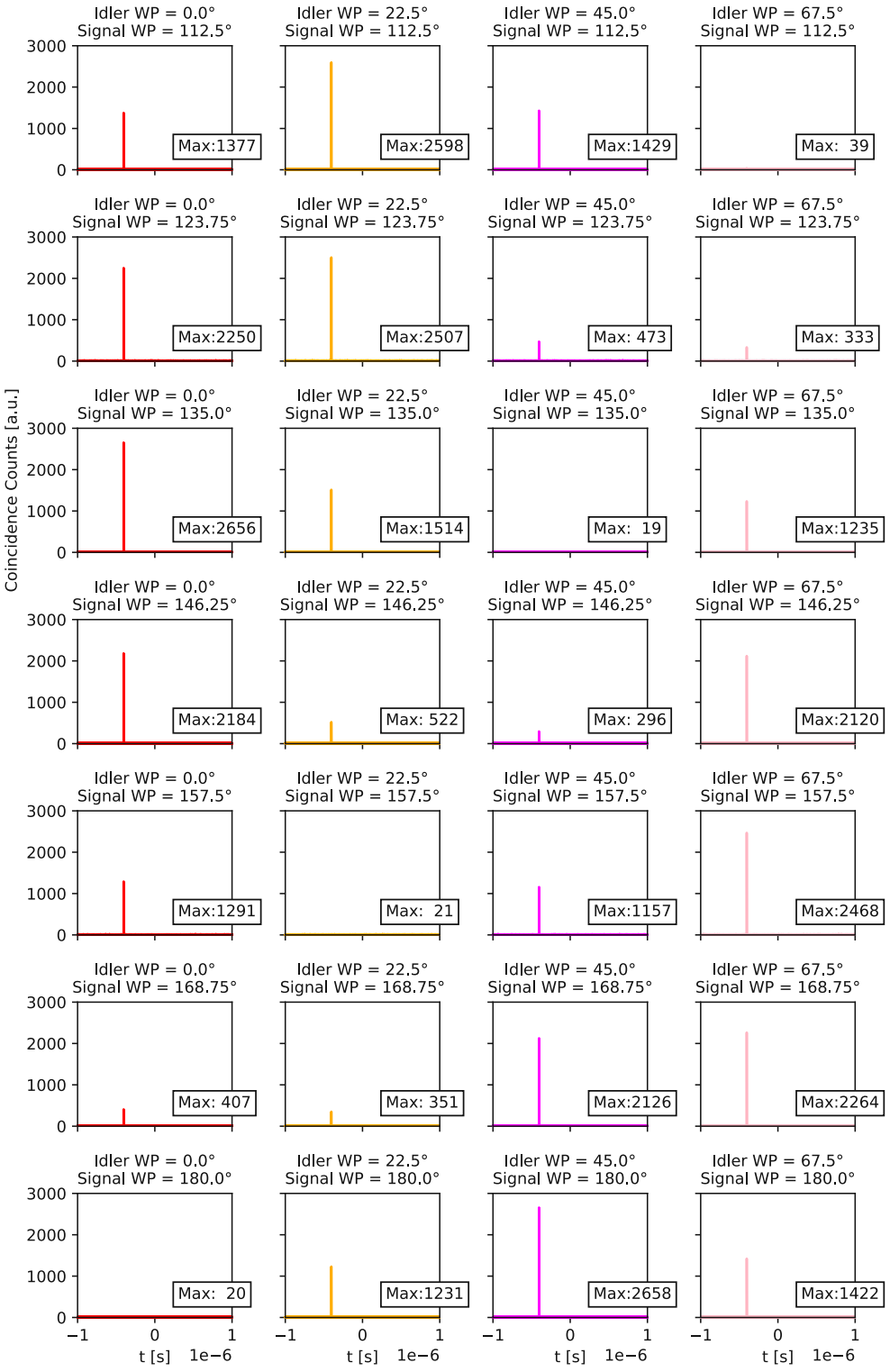

These 68 individual maximum coincidence counts are then used to construct the CHSH

curve. The maximum coincidence peak values for a full dataset appear consistently at the same time delay. As shown in the figure on the last three pages, the coincidence peak is detected at 403.7 ns. The coincidence peaks for each waveplate combination are extracted and plotted, resulting in four distinct curves with the same idler angle setting. In Figure 14, the coincidence peaks are plotted as a function of the signal waveplate angle, with the idler angle fixed. As predicted by theory, a cosine-squared curve is expected.

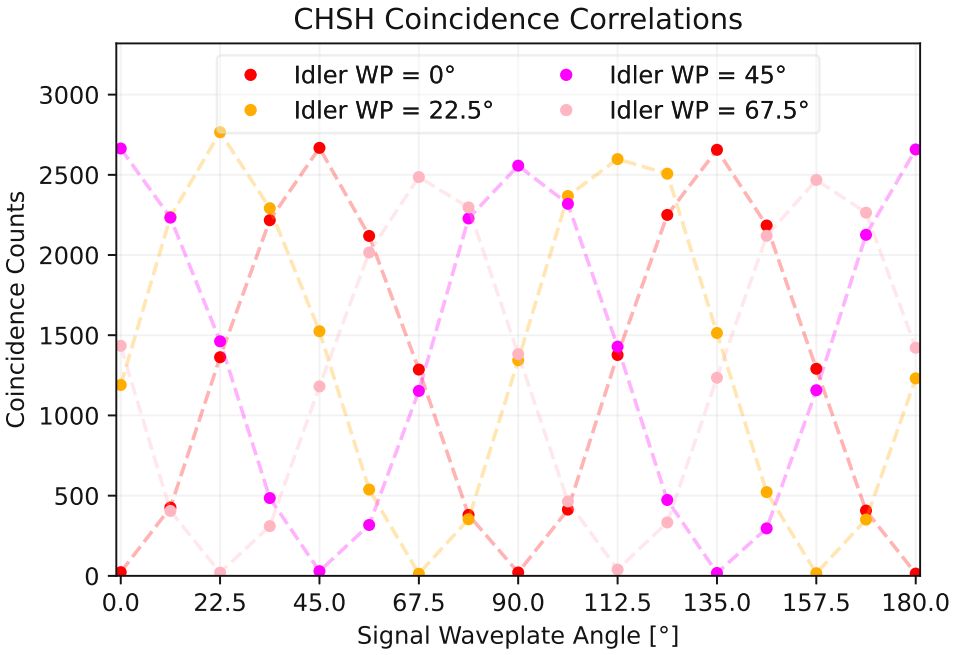

Figure 14: Coincidence counts for all waveplate settings combinations, with points directly connected, exhibiting a cosine-squared pattern.

Consequently, the data points are fitted with a cosine-squared function. This fitting approach facilitates a more reliable extraction result. Since the S-value estimation is based only on 16 points, a single deviation can strongly influence the result. However, fitting the data using 68 data points produces more reliable results and offers a smoother visualization without requiring additional intermediate angle settings.

To calculate the S-value, additional steps are required. Since the polarization rotation is doubled due to the rotating waveplates, all angles must be divided by 2. These angles are then given in degrees as:

$$S = E(0°, 11.25°) - E(0°, 33.75°) + E(22.5°, 11.25°) + E(22.5°, 33.75°).$$

Each expectation value for the S-value is computed from coincidence counts. The general formula for the expectation is given by:

$$E(a,b) = \frac{C(a,b) - C(a,b_\perp) - C(a_\perp,b) + C(a_\perp,b_\perp)}{C(a,b) + C(a,b_\perp) + C(a_\perp,b) + C(a_\perp,b_\perp)},$$

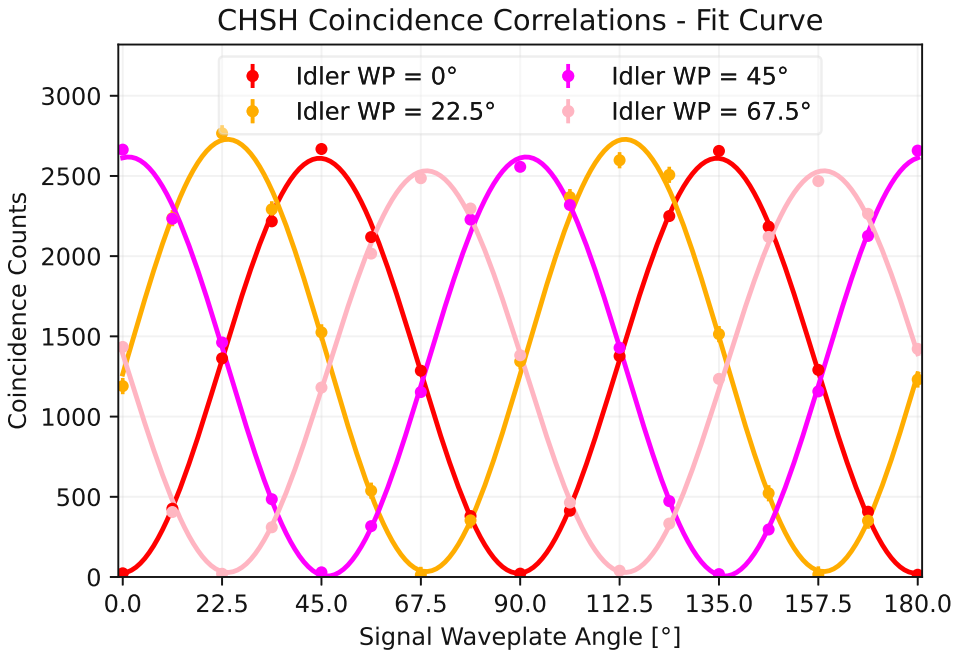

Figure 15: Coincidence counts for all waveplate combinations, including a cosine-squared fit and error bars.

where $a_\perp = a + 45°$, and similarly for $b_\perp$.

$$E(0°, 11.25°) = \frac{C(0°, 11.25°) - C(0°, 56.25°) - C(45°, 11.25°) + C(45°, 56.25°)}{C(0°, 11.25°) + C(0°, 56.25°) + C(45°, 11.25°) + C(45°, 56.25°)},$$

$$E(0°, 33.75°) = \frac{C(0°, 33.75°) - C(0°, 78.75°) - C(45°, 33.75°) + C(45°, 78.75°)}{C(0°, 33.75°) + C(0°, 78.75°) + C(45°, 33.75°) + C(45°, 78.75°)},$$

$$E(22.5°, 11.25°) = \frac{C(22.5°, 11.25°) - C(22.5°, 56.25°) - C(67.5°, 11.25°) + C(67.5°, 56.25°)}{C(22.5°, 11.25°) + C(22.5°, 56.25°) + C(67.5°, 11.25°) + C(67.5°, 56.25°)},$$

$$E(22.5°, 33.75°) = \frac{C(22.5°, 33.75°) - C(22.5°, 78.75°) - C(67.5°, 33.75°) + C(67.5°, 78.75°)}{C(22.5°, 33.75°) + C(22.5°, 78.75°) + C(67.5°, 33.75°) + C(67.5°, 78.75°)}.$$

Based on the fitted curve, 16 points corresponding to the angle combinations with the potential for maximal violation are extracted. Using the fitted points shown in Figure 16, the calculated S-value, as the final result of this Bell parameter analysis, is given by:

$$S = 2.7757 \pm 0.0209\,.$$

where ± 0.0209 represents the error estimation. This result clearly violates the classical bound of $S \leq 2$, which confirms quantum entanglement.

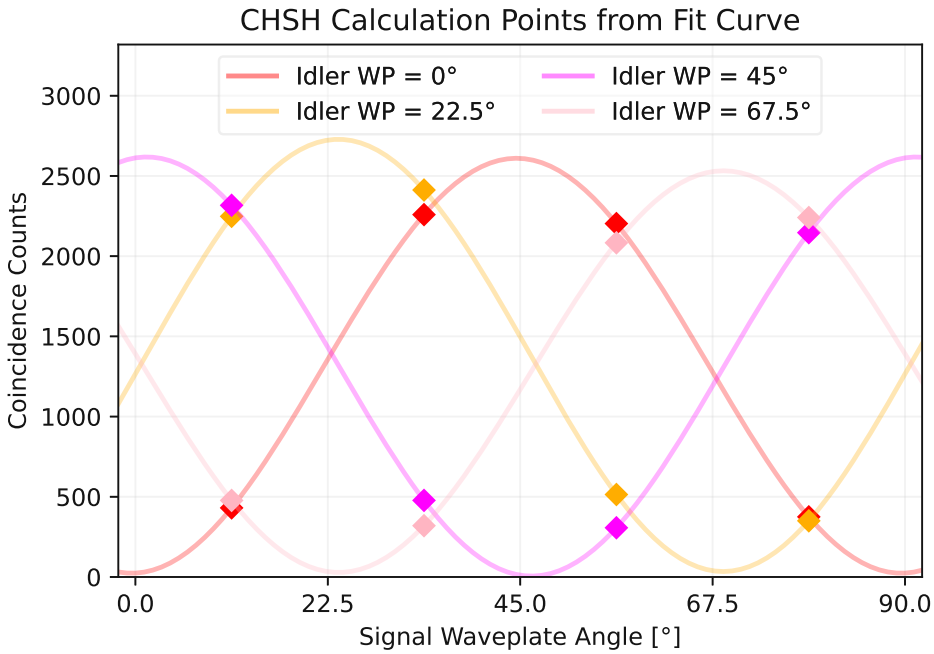

Figure 16: Data points at the 16 angle combinations with the potential for maximal violation, estimated from the fitted curves.

Fidelity

Since there is no full quantum state tomography performed, approximate quantum fidelity bounds are estimated. The source produces a $|\Phi^+\rangle$ Bell state, which is the target state. Therefore, the density matrix ρ is reconstructed from the measurements.

$$F = Tr[|\Phi^+\rangle\langle\Phi^+|\,\rho\,|\Phi^+\rangle\langle\Phi^+|]$$

$$= Tr\left[\frac{1}{\sqrt{2}}\begin{bmatrix}1\\0\\0\\1\end{bmatrix}\frac{1}{\sqrt{2}}\begin{bmatrix}1&0&0&1\end{bmatrix}\begin{bmatrix}\rho_{11}&\rho_{12}&\rho_{13}&\rho_{14}\\\rho_{21}&\rho_{22}&\rho_{23}&\rho_{24}\\\rho_{31}&\rho_{32}&\rho_{33}&\rho_{34}\\\rho_{41}&\rho_{42}&\rho_{43}&\rho_{44}\end{bmatrix}\frac{1}{\sqrt{2}}\begin{bmatrix}1\\0\\0\\1\end{bmatrix}\frac{1}{\sqrt{2}}\begin{bmatrix}1&0&0&1\end{bmatrix}\right]$$

$$= \frac{1}{4}Tr\left[\begin{bmatrix}1&0&0&1\\0&0&0&0\\0&0&0&0\\1&0&0&1\end{bmatrix}\begin{bmatrix}\rho_{11}&\rho_{12}&\rho_{13}&\rho_{14}\\\rho_{21}&\rho_{22}&\rho_{23}&\rho_{24}\\\rho_{31}&\rho_{32}&\rho_{33}&\rho_{34}\\\rho_{41}&\rho_{42}&\rho_{43}&\rho_{44}\end{bmatrix}\begin{bmatrix}1&0&0&1\\0&0&0&0\\0&0&0&0\\1&0&0&1\end{bmatrix}\right]$$

$$= \frac{1}{4}Tr\left[\begin{bmatrix}\rho_{11}+\rho_{14}+\rho_{41}+\rho_{44}&0&0&\rho_{11}+\rho_{14}+\rho_{41}+\rho_{44}\\0&0&0&0\\0&0&0&0\\\rho_{11}+\rho_{14}+\rho_{41}+\rho_{44}&0&0&\rho_{11}+\rho_{14}+\rho_{41}+\rho_{44}\end{bmatrix}\right]$$

$$= \frac{1}{2}(\rho_{11}+\rho_{44}+\rho_{41}+\rho_{14})\,.$$

The terms ρ_{11} and ρ_{44} correspond directly to the probabilities of measuring in the $|\mathrm{HH}\rangle$ and $|\mathrm{VV}\rangle$ states, respectively. Specifically,

$$\rho_{11} = \langle \mathrm{HH}|\rho|\mathrm{HH}\rangle, \quad \rho_{44} = \langle \mathrm{VV}|\rho|\mathrm{VV}\rangle.$$

To estimate these probabilities from the experimental data, coincidence counts are normalized as follows:

$$\rho_{ij} = \frac{C_{ij}}{N},$$

where C_{ij} is the number of coincidence counts corresponding to the outcome measured in the basis ij, and the normalization constant N is:

$$N = C_{\mathrm{HH}} + C_{\mathrm{VV}} + C_{\mathrm{DD}} + C_{\mathrm{AA}}\,.$$

For off-diagonal elements ρ_{14} and ρ_{41}, measurements in the diagonal and anti-diagonal bases are required. A brief recap of the combined two-qubit basis states in these bases:

$$|\mathrm{DD}\rangle = |\mathrm{D}\rangle \otimes |\mathrm{D}\rangle = \frac{1}{\sqrt{2}}\begin{bmatrix}1\\1\end{bmatrix} \otimes \frac{1}{\sqrt{2}}\begin{bmatrix}1\\1\end{bmatrix} = \frac{1}{2}\begin{bmatrix}1\\1\\1\\1\end{bmatrix},$$

$$|\mathrm{AA}\rangle = |\mathrm{A}\rangle \otimes |\mathrm{A}\rangle = \frac{1}{\sqrt{2}}\begin{bmatrix}1\\-1\end{bmatrix} \otimes \frac{1}{\sqrt{2}}\begin{bmatrix}1\\-1\end{bmatrix} = \frac{1}{2}\begin{bmatrix}1\\-1\\-1\\1\end{bmatrix}.$$

A detailed analysis of the diagonal coincidence values requires examining the probability of coincidence in the diagonal basis. The probability of finding the system in the state $|\mathrm{DD}\rangle$ is given by:

$$\langle \mathrm{DD}|\rho|\mathrm{DD}\rangle = \frac{1}{2}\begin{bmatrix}1 & 1 & 1 & 1\end{bmatrix}\begin{bmatrix}\rho_{11} & \rho_{12} & \rho_{13} & \rho_{14}\\ \rho_{21} & \rho_{22} & \rho_{23} & \rho_{24}\\ \rho_{31} & \rho_{32} & \rho_{33} & \rho_{34}\\ \rho_{41} & \rho_{42} & \rho_{43} & \rho_{44}\end{bmatrix}\frac{1}{2}\begin{bmatrix}1\\1\\1\\1\end{bmatrix}$$

$$= \frac{1}{4}\begin{bmatrix}1 & 1 & 1 & 1\end{bmatrix}\begin{bmatrix}\rho_{11}+\rho_{12}+\rho_{13}+\rho_{14}\\ \rho_{21}+\rho_{22}+\rho_{23}+\rho_{24}\\ \rho_{31}+\rho_{32}+\rho_{33}+\rho_{34}\\ \rho_{41}+\rho_{42}+\rho_{43}+\rho_{44}\end{bmatrix}$$

$$= \frac{1}{4}\left(\rho_{11}+\rho_{12}+\rho_{13}+\rho_{14}+\rho_{21}+\rho_{22}+\rho_{23}+\rho_{24}+\rho_{31}+\rho_{32}+\rho_{33}+\rho_{34}+\rho_{41}+\rho_{42}+\rho_{43}+\rho_{44}\right).$$

Similarly, for the antidiagonal basis, the probability of coincidence is:

$$\langle \mathrm{AA}|\rho|\mathrm{AA}\rangle = \frac{1}{2}\begin{bmatrix}1 & -1 & -1 & 1\end{bmatrix}\begin{bmatrix}\rho_{11} & \rho_{12} & \rho_{13} & \rho_{14}\\ \rho_{21} & \rho_{22} & \rho_{23} & \rho_{24}\\ \rho_{31} & \rho_{32} & \rho_{33} & \rho_{34}\\ \rho_{41} & \rho_{42} & \rho_{43} & \rho_{44}\end{bmatrix}\frac{1}{2}\begin{bmatrix}1\\-1\\-1\\1\end{bmatrix}$$

$$= \frac{1}{4}\begin{bmatrix}1 & -1 & -1 & 1\end{bmatrix}\begin{bmatrix}\rho_{11}-\rho_{12}-\rho_{13}+\rho_{14}\\ \rho_{21}-\rho_{22}-\rho_{23}+\rho_{24}\\ \rho_{31}-\rho_{32}-\rho_{33}+\rho_{34}\\ \rho_{41}-\rho_{42}-\rho_{43}+\rho_{44}\end{bmatrix}$$

$$= \frac{1}{4}\left(\rho_{11}-\rho_{12}-\rho_{13}+\rho_{14}-\rho_{21}+\rho_{22}+\rho_{23}-\rho_{24}-\rho_{31}+\rho_{32}+\rho_{33}-\rho_{34}+\rho_{41}-\rho_{42}-\rho_{43}+\rho_{44}\right).$$

Summing $\langle \mathrm{AA}|\rho|\mathrm{AA}\rangle + \langle \mathrm{DD}|\rho|\mathrm{DD}\rangle$ and normalizing it allows extraction of the off-diagonal elements ρ_{14} and ρ_{41} of the density matrix. This leads to the following expression:

$$\frac{C_{\mathrm{DD}}+C_{\mathrm{AA}}}{N} = \frac{1}{2}(\rho_{11}+\rho_{14}+\rho_{22}+\rho_{23}+\rho_{32}+\rho_{33}+\rho_{41}+\rho_{44})$$

It is known that the normalized diagonal elements satisfy the trace condition:

$$Tr(\rho) = \rho_{11}+\rho_{22}+\rho_{33}+\rho_{44} = 1\,.$$

By applying the trace condition, the expression simplifies to:

$$\frac{C_{\mathrm{DD}}+C_{\mathrm{AA}}}{N} = \frac{1+\rho_{14}+\rho_{23}+\rho_{32}+\rho_{41}}{2}.$$

By rearranging the terms, the missing off-diagonal elements can be expressed as:

$$\rho_{14}+\rho_{41} = \frac{2C_{\mathrm{DD}}+2C_{\mathrm{AA}}}{N} - 1 - \rho_{23} - \rho_{32}\,.$$

Then substituting this into the Fidelity, results in:

$$F = \frac{1}{2}\left[\frac{C_{\mathrm{HH}}}{N}+\frac{C_{\mathrm{VV}}}{N}+\frac{2C_{\mathrm{DD}}+2C_{\mathrm{AA}}}{N} - 1 - \rho_{23} - \rho_{32}\right]$$

$$= \frac{C_{\mathrm{HH}}+C_{\mathrm{VV}}+2C_{\mathrm{DD}}+2C_{\mathrm{AA}}}{2N} - \frac{1+\rho_{23}+\rho_{32}}{2}.$$

Finally, by applying the Cauchy–Schwarz inequality in a finite-dimensional complex Hilbert space, the off-diagonal elements of a density matrix satisfy $|\rho_{ij}|^2 \leq \rho_{ii}\rho_{jj}$, or equivalently, $|\rho_{ij}| \leq \sqrt{\rho_{ii}\rho_{jj}}$. By substituting the diagonal elements ρ_{22} and ρ_{33} with the appropriately normalized coincidence counts C_{HV} and C_{VH}, respectively, the fidelity bounds are obtained as:

$$\frac{C_{\mathrm{HH}}+C_{\mathrm{VV}}+2C_{\mathrm{DD}}+2C_{\mathrm{AA}}-2\sqrt{C_{\mathrm{HV}}C_{\mathrm{VH}}}}{2N} - \frac{1}{2}$$

$$\leq F \leq$$

$$\frac{C_{\mathrm{HH}}+C_{\mathrm{VV}}+2C_{\mathrm{DD}}+2C_{\mathrm{AA}}+2\sqrt{C_{\mathrm{HV}}C_{\mathrm{VH}}}}{2N} - \frac{1}{2}.$$

A similar result is obtained for the second inequality. The fidelity bounds are determined by taking the lower minimum and the upper maximum values.

Error estimation

A closer look at the error estimation for each point is presented. In the upcoming CHSH curve plots, there are error bars, which provide the uncertainty of the measurement. Two imprecision factors are taken into account in the derivation. First, the statistical fluctuation for counting photon coincidences and second the mechanical uncertainties of the rotating waveplates.

For counting photon coincidences, the poisson standard deviation [27] must be taken into account, which is defined as:

$$\sigma_{poisson} = \sqrt{C}\,,$$

where C are the coincidence counts. This captures the fluctuations of the discrete single-photon detection. The rotators have a specified manufacturing uncertainty [1] of $\sigma_{angle} = 0.14°$. The angular uncertainty propagates through the fitting function. The differential error propagation is calculated as follows:

$$\sigma_{angle}(\theta) = \left|\frac{\partial f_{fitting}(\theta)}{\partial \theta}\right| \sigma_{angle}\,.$$

The first step is to differentiate the cosine-squared fitting function. The function $f_{fitting}$, is defined as:

$$f_{fitting}(\theta) = a\cos^2\left((2\theta - \phi)\,\frac{\pi}{180}\right) + b,$$

where θ is the angle, ϕ is the phase shift in degrees, a the amplitude, and b an offset. As already discovered, 2θ is used in the fitting function because the polarization direction of the photon rotates twice the angle.
Differentiating with respect to θ, applying the chain rule and using the double angle identity $\sin(2x) = 2\sin(x)\cos(x)$:

$$\begin{aligned}\frac{d}{d\theta} f_{fitting}(\theta) &= 2a\cos\left((2\theta - \phi)\,\frac{\pi}{180}\right)\frac{d}{d\theta}\left(\cos\left((2\theta - \phi)\,\frac{\pi}{180}\right)\right)\\ &= -2a\cos\left((2\theta - \phi)\,\frac{\pi}{180}\right)\sin\left((2\theta - \phi)\,\frac{\pi}{180}\right)\frac{2\pi}{180}\\ &= -a\frac{2\pi}{180}\sin\left(2\,(2\theta - \phi)\,\frac{\pi}{180}\right).\end{aligned}$$

The total error propagation becomes:

$$\sigma_{total}(\theta) = \sqrt{\sigma^2_{poission} + \left(\left|\frac{d}{d\theta} f(\theta)\right| \sigma_{angle}\right)^2}\,.$$

This error propagation is also done for the expectation values in the same way.

[1] Motorized Cage Rotator Manual. Accessed on 20.08.2025.
Link: https://www.thorlabs.com/newgrouppage9.cfm?objectgroup_id=8750

5 Results

This chapter presents the individual experimental setups and results for the conducted experiments. The first section provides results for different field-deployed paths. The second section introduces the APC system and the impact of path switching. The third section presents a long-term evaluation with and without APC for single paths and path switching. The final section offers an overview of the impact of classical channels co-propagating with a quantum signal on the same fiber.

Initial Experimental Setup Structure

The initial setup, shown in Figure 17, serves as the starting point of all different experiments conducted in this work. This setup also serves as a reference point for calibration, as the signal path is local within the lab and is unaffected by field-deployed fiber.

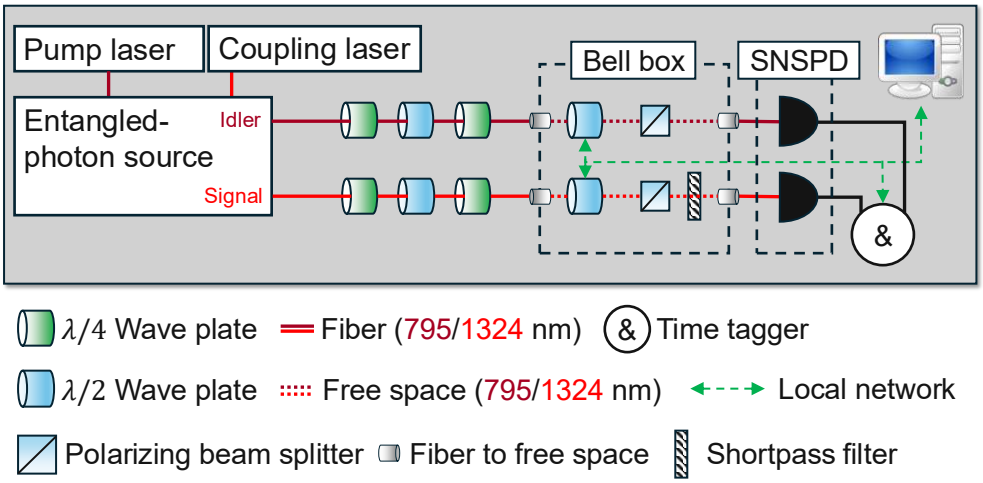

Figure 17: Initial experimental setup structure.

This setup was also used to generate the measurement data in section 4.2. For system calibration, a polarization controller is employed for each path. The polarization controller consists of two quarter-waveplates and one half-waveplate, enabling polarization manipulation to any arbitrary point on the Poincaré sphere. This process ensures that the polarization state received at the Bell box is maximally entangled. Without the use of a polarization-maintaining fiber, this is crucial to overcome any polarization drifts induced by the short setup fibers. However, the fact that this procedure must be done by hand with every setup change is a minor limitation.

5.1 Distance Limits

In this section, research question I. is addressed. For the characterization of the entangled photon distributed over different paths, an APC system is added to the experimental setup, illustrated in Figure 18. This extension eliminates the need for recalibration of the polarization controller every time the field-deployed fiber is changed. Only after the installation of the APC system is a manual calibration required. After that, any polarization changes between the APC injector and the APC compensator can be disregarded. This means that polarization changes induced by another fiber are automatically compensated by triggering the APC. For measurement simplification, the end nodes are looped, and the distributed signal photons return to the laboratory. Although this contradicts the network structure for a future quantum network, it offers other advantages at this stage of research. The most noticeable advantage is that only one photon detection system is needed, i.e., it requires a single cooling scheme, and the distributed path length is doubled. The characterization

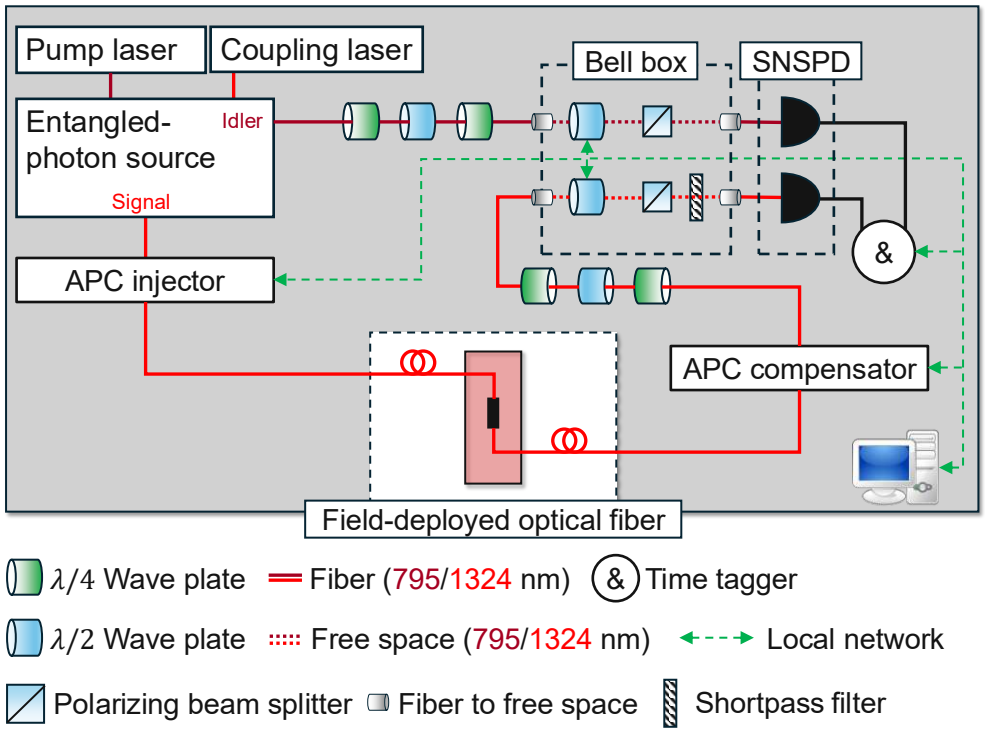

Figure 18: Experimental structure with an APC system designed for distributing polarization-entangled photons along a field-deployed path.

of the fiber network is already explained in section 3.4, illustrated in Figure 8. Since the entire entanglement characterization procedure depends on the single-photon count, it can be predicted that fiber attenuation plays a major role, especially with very low quantum signal power. CHSH measurements were conducted for different paths and confirmed the quantum entanglement distribution. The results for 15 km, 30 km and 100 km are shown in Figure 19, 20, and 21, respectively. It yields a measured S-value of $S = 2.69$ and a

fidelity between $96.71\% \leq F \leq 99.28\%$ for the 15 km field-deployed fiber path.

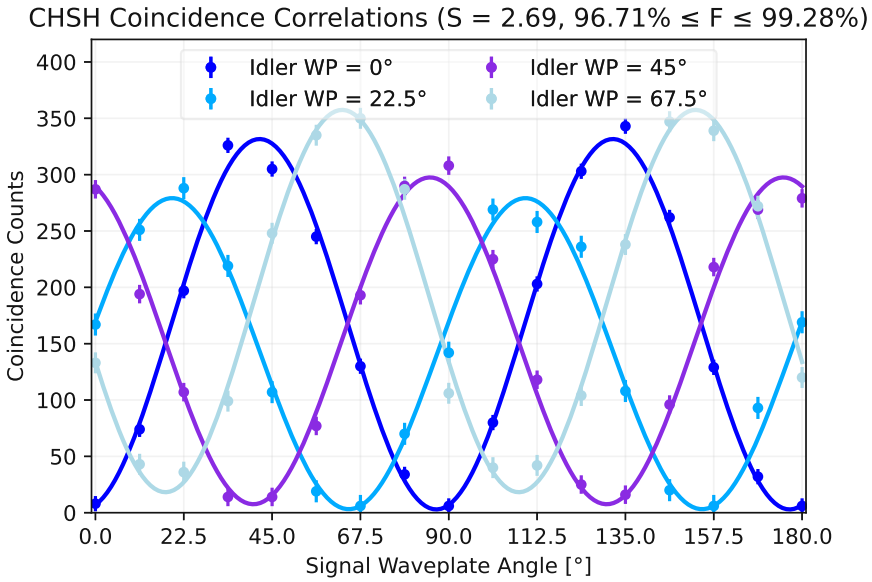

Figure 19: Coincidence counts as a function of the signal waveplate angle, over a 15 km path.

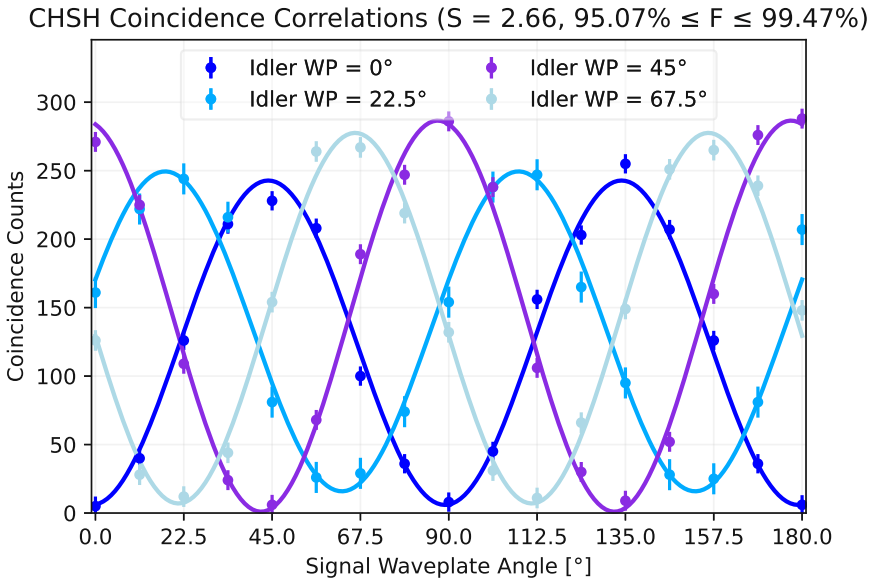

Figure 20: Coincidence counts as a function of the signal waveplate angle, over a 30 km path.

For these two paths, the measurement was performed with the same configuration settings. With an integration time of 1 second, a clear coincidence peak is generated from more than 300 single-photon counts. Longer paths, such as 100 km, required a longer integration time of 30 seconds and maximal pump laser power. This shows a result of $S = 2.49$ and a fidelity between $89.82\% \leq F \leq 98.55\%$. Shown in Figure 21, the maximal coincidence

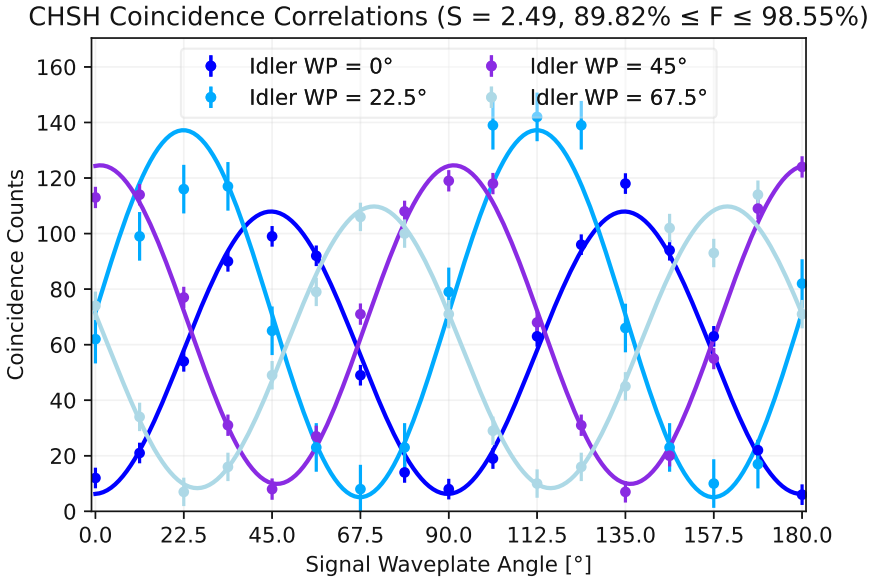

Figure 21: Coincidence counts as a function of the signal waveplate angle, with each waveplate configuration having a 30 second integration time, over a 100 km path.

peaks reach only 140 single-photon counts. This is due to the high attenuation of the path, resulting in very low single-photon detection. Without sufficiently long integration time, coincidence peaks either do not appear or are hidden by noise. Without coincidence peaks, it is impossible to estimate or confirm a violation of the Bell inequality.

5.2 Dynamic Switching

To address research question II., the experimental setup has been expanded. A mechanical optical switch and a beam splitter were gradually integrated, in between the APC system. Manual calibration is not required, as the components are positioned after the APC injector and before the APC compensator. The mechanical optical switch, controlled by the data acquisition procedure, directs the quantum signal along two different field-deployed paths for the signal photon. The beam splitter then recombines the two paths, resulting in a loss of photons. The extended setup is shown in Figure 22.

New challenges arise because these two paths have entirely different effects, such as attenuation and polarization shift. If a calibration is performed manually for one path, the polarization changes completely after switching paths. Consequently, entangled photons

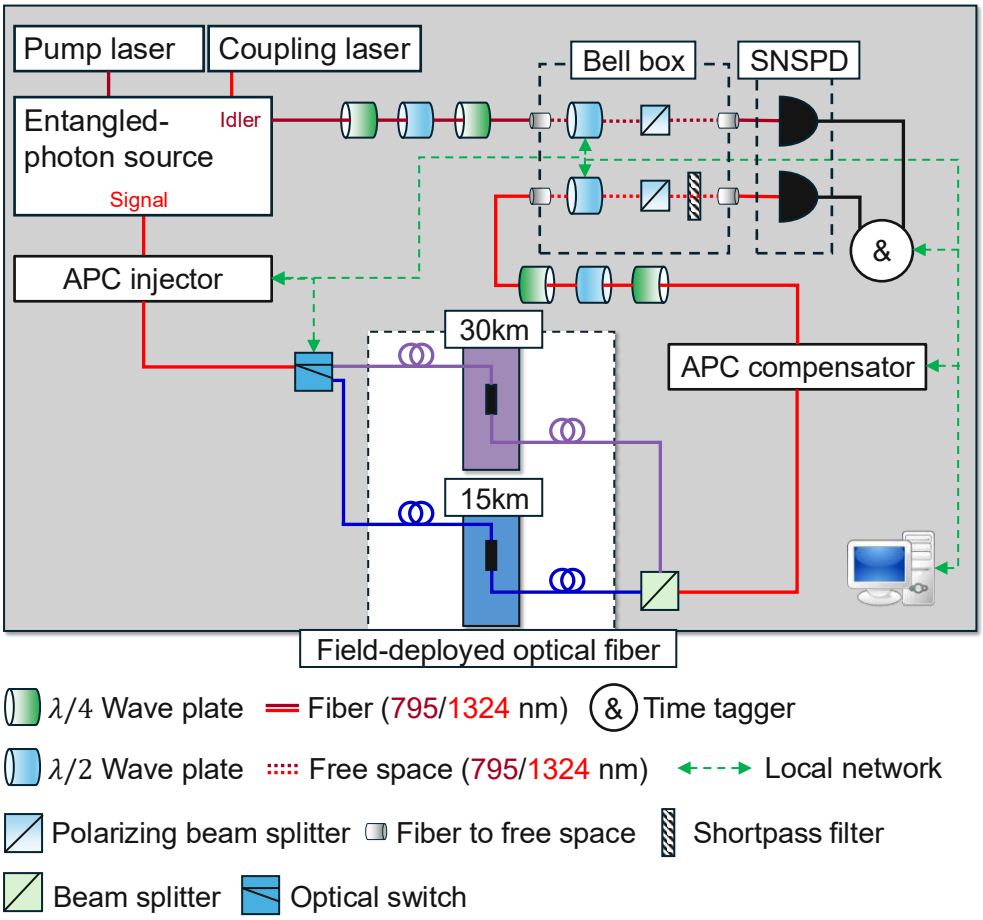

Figure 22: Experimental structure designed for distributing polarization-entangled photons and switching between two field-deployed paths.

can be distributed and confirmed only along the calibrated path. Individual paths influence the polarization of the photons differently, leading to a loss of observable entanglement by the CHSH measurement after uncompensated path changes. To overcome individual shifts on each path, compensation from the APC system is necessary for every path switching event. To illustrate the impact of a path switch, the classical fidelity, measured by the APC is shown in Figure 23. The periodic path switching events clearly show a drop in the classical fidelity under 50%.

In the initial state of these experiments, one path is local (using the optical switch operation mode explained in section 3.6), while the other follows a deployed fiber path. This setup already demonstrates how the APC system can handle two completely different polarization shifts. After completing a full CHSH measurement on the local path, the path is switched to the field-deployed one, and the measurement continues there. The S-value and fidelity for the two different path impacts can then be shown without requiring any manual adjustments. After demonstrating path switching with one path still local, the

next step, as shown in Figure 22, involves switching between two field-deployed paths. The figure presents an example with paths of 15 km and 30 km, though this can be applied to any field-deployed path. To provide a clearer visualization of the experimental results, the S-value and fidelity are presented over time in the following section.

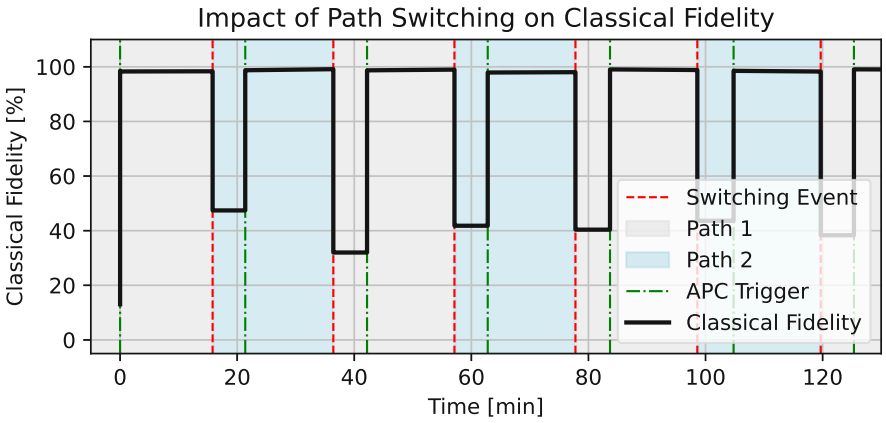

Figure 23: Classical fidelity over time for periodic path switching events measured by the APC system.

5.3 Long Time Evaluation

This section is divided into three phases. The characterization of the entanglement distribution is shown under different setups, over long time periods of hours or days. Therefore, the S-value and fidelity, including error bounds, are plotted over time. In the first phase, the entanglement distribution is shown over a single path. The second phase demonstrates switching between a local path and a field-deployed fiber. Finally, the switching is demonstrated over two different paths.

In the first phase, the importance of the APC over time is highlighted, especially for field-deployed fibers.

Single field-deployed path evaluation

To address the main differences between lab conditions and urban setups two experiments are conducted based on the setups shown in Figure 17 and 18 (with the APC switched off). In the experiment with the local path, the S-value remains stable for a period of 8 days, as shown in Figure 24. In contrast, the distribution over the field-deployed path, with the APC switched off, shows a drift in both the S-value and fidelity, illustrated in Figure 25. This drift in characterization of the entanglement is a consequence of the polarization drift. With the APC turned on and triggered after every complete measurement, the polarization remains stable. Due to the slight drift over time, polarization compensation requires only milliseconds and does not significantly increase downtime in the network.

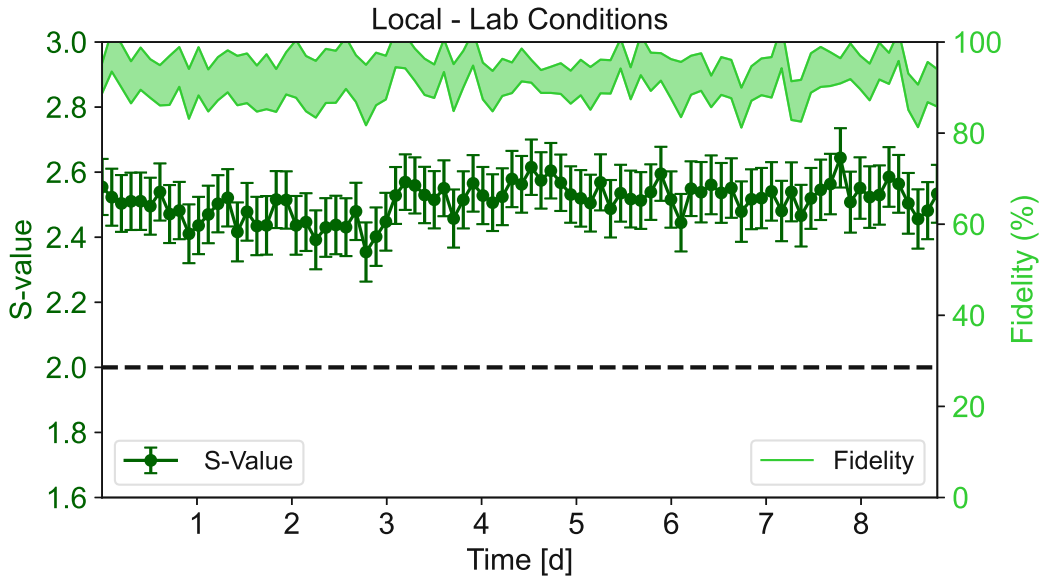

Figure 24: S-value evaluation over 8 days without the APC under local lab conditions.

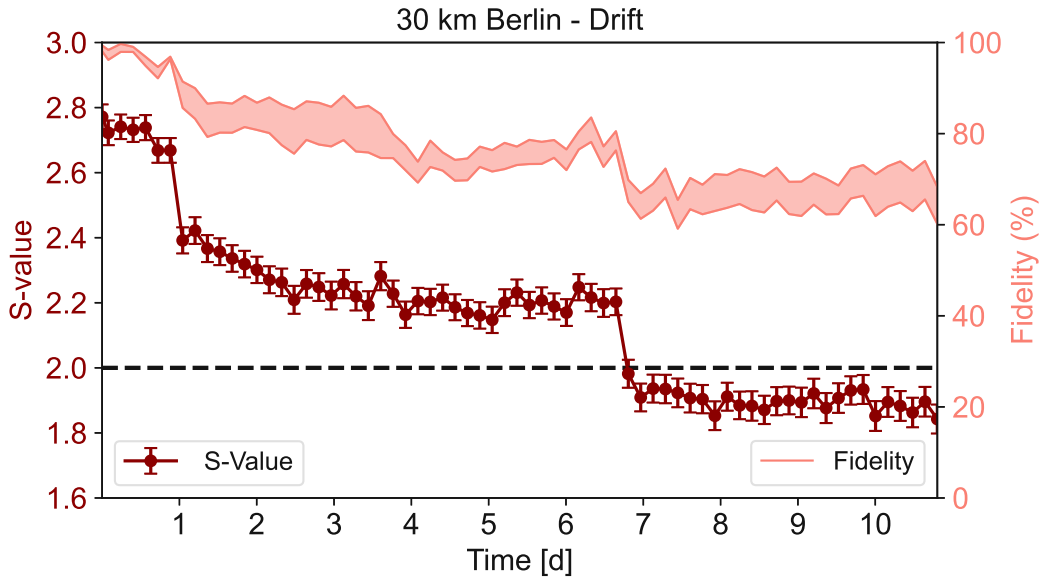

Figure 25: S-value drift caused by polarization changes in a 30 km field-deployed fiber over a period of 10 days.

Switching between local and field paths

Moving into the second phase, switching between the local path and the field-deployed fiber was performed. These path switching experiments are conducted over a local path and 15, 30, and 60 km respectively. The results for the 30 km path, illustrated in Figure 26, are divided into two plots.

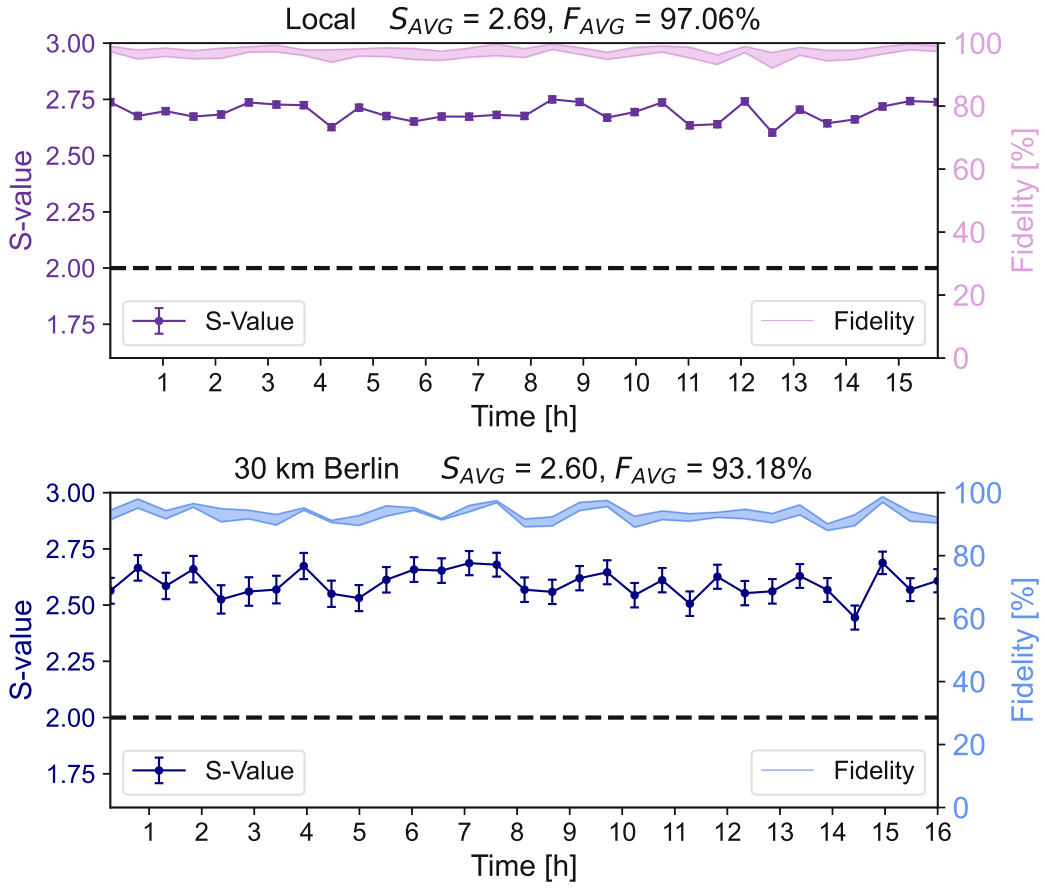

Figure 26: Long-term S-value and fidelity evaluation with switching between local (top) and 30 km field deployed fiber (bottom) path.

The upper plot shows an average S-value of $S_{AVG} = 2.69$ and fidelity $F_{AVG} = 97.06\%$ for the local path, while the lower plot displays those for the 30 km field-deployed fiber path, resulting in an average S-value of $S_{AVG} = 2.60$ and fidelity of $F_{AVG} = 93.18\%$. As seen in Figure 26, the exact time, where a measurement was performed, alternates between the paths. The results for the 15 and 60 km distances show similar outcomes and are therefore not explicitly plotted.

Switching between two different field paths

For the final step, which is the closest stage to a real quantum network reached in this work, the entanglement distribution was performed over two different paths. With a more customizable optical switching system, the entanglement distribution can be easily confirmed over a range of different paths simply by selecting the desired switch position.

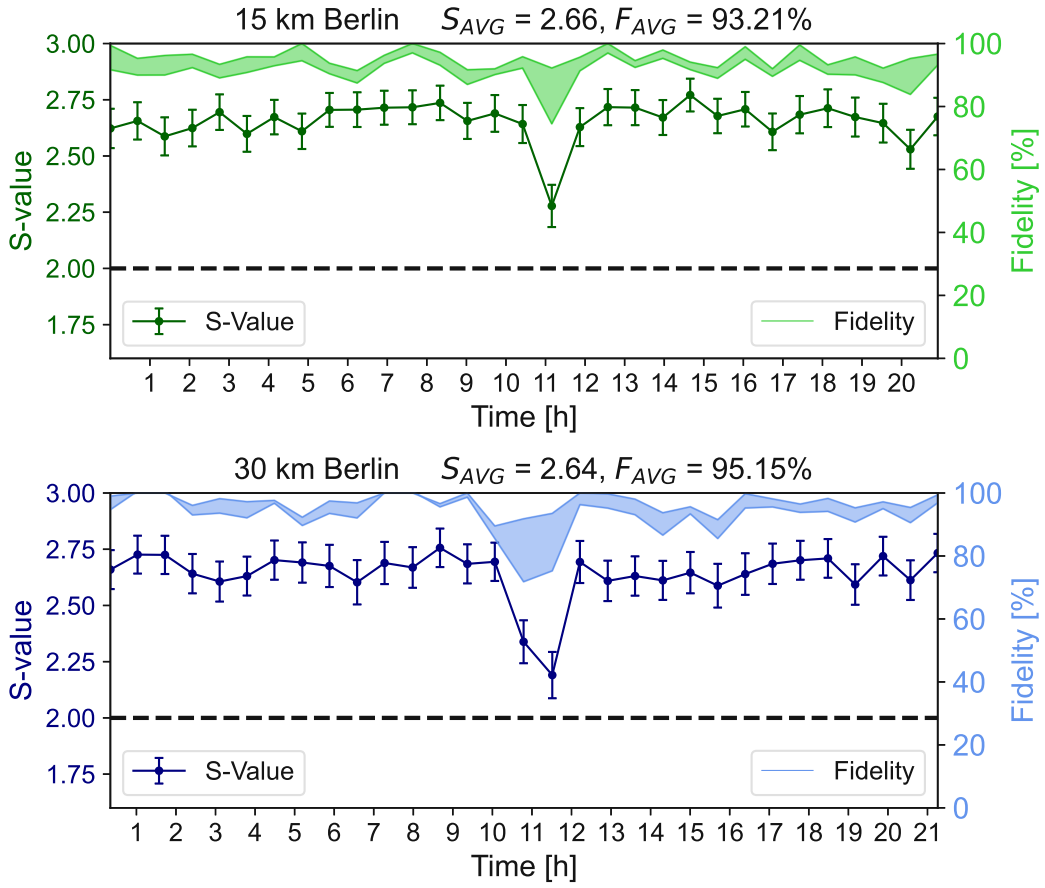

Figure 27: Long-term S-value and fidelity evaluation with switching between 15 km (top) and 30 km field deplyed fiber (bottom) path.

The upper plot shows an average S-value of $S_{AVG} = 2.66$ and fidelity $F_{AVG} = 93.21\%$ for the 15 km path, while the lower plot shows those for the 30 km field-deployed fiber path, results in an average S-value of $S_{AVG} = 2.64$ and fidelity of $F_{AVG} = 95.15\%$.

5.4 Impact of Classical Light

To characterize the operation of a hybrid quantum-classical network as proposed in research question IV., experiments were carried out to show the crosstalk between the signals. In the first phase the setup was expanded with an OADM and noise shaped 50-GHz wide channels (explained in section 3.7 to emulate classical light). The setup shown in Figure 28, investigates the impact of different single channels, as well as the impact of path switching and coexistence of classical light together [41], setup illustrated in Figure 33. In the second phase, a real 50-GHz dense wavelength-division multiplexing (DWDM) channel and an optical filter were used to suppress the noise floor. Each illustrated S-value consists of an average of five complete CHSH measurements with the same settings.

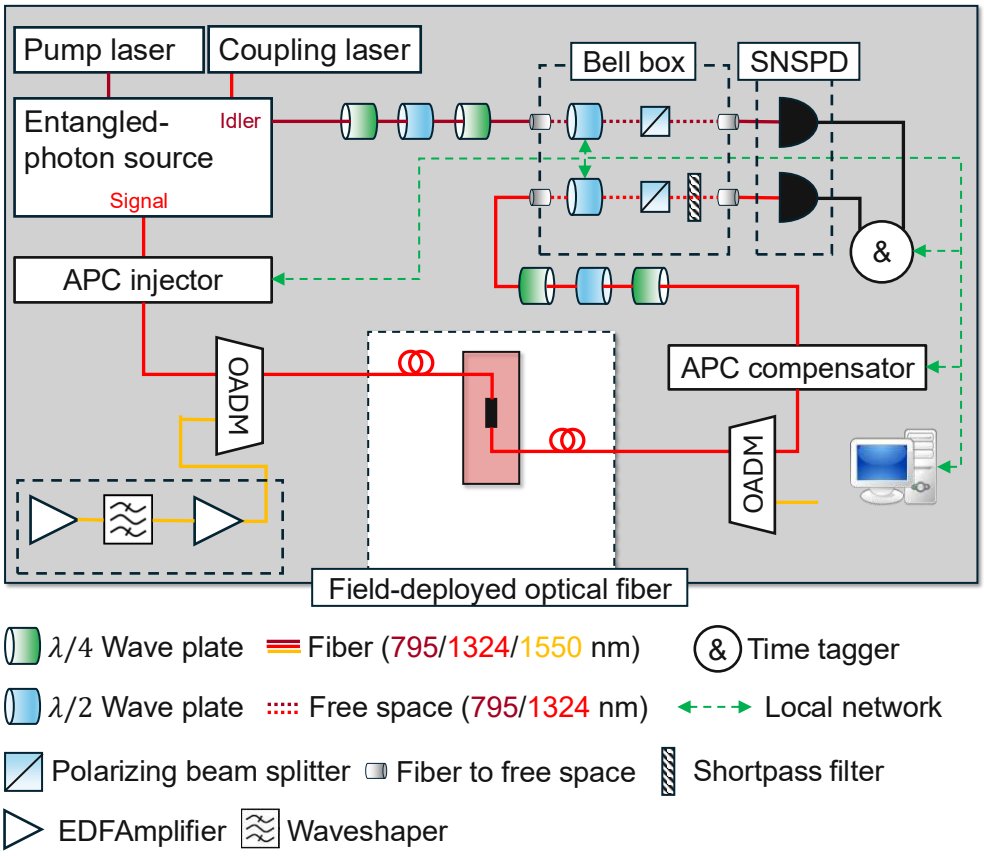

Figure 28: Experimental structure designed for multiplexing classical and quantum signals over a single field deployed path.

In the first experiment, CHSH measurements were carried out, with co-propagating amplified spontaneous emission (ASE) noise shaped into 50-GHz wide channels. Measurements were conducted through the 30 km fiber loop while varying the launch power of the single 50-GHz ITU-T channel CH31 (1552.5 nm, 193.1 THz) from -6 dBm to -1.5 dBm (total spectrum power of 0 dBm to 6 dBm). The resulting spectrograms, shown in Figure 29, are

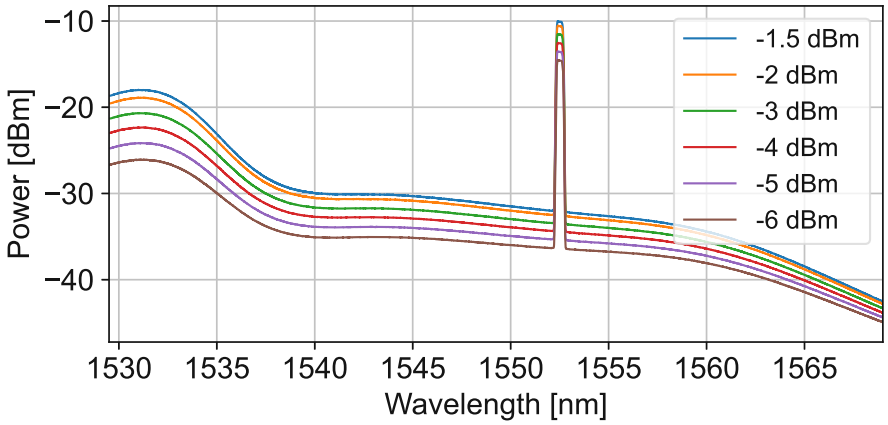

Figure 29: Transmitted optical spectra for varying classical channel power. Measurement performed with a resolution bandwidth (RBW) of 0.1nm.

measured before the classical signal is routed to the OADM.

The measured S-value decreases with increasing classical signal power, as shown in Figure 30. It is a trade-off between the total power of the classical signal and the perceived entanglement quality. This is due to increased noise levels that prevent the precise measurement of entangled photons. In the operational range ≤ -1.5 dBm classical light power, the classical limit of $S = 2$ is never crossed, where quantum entanglement can no longer be verified (without adding additional filtering).

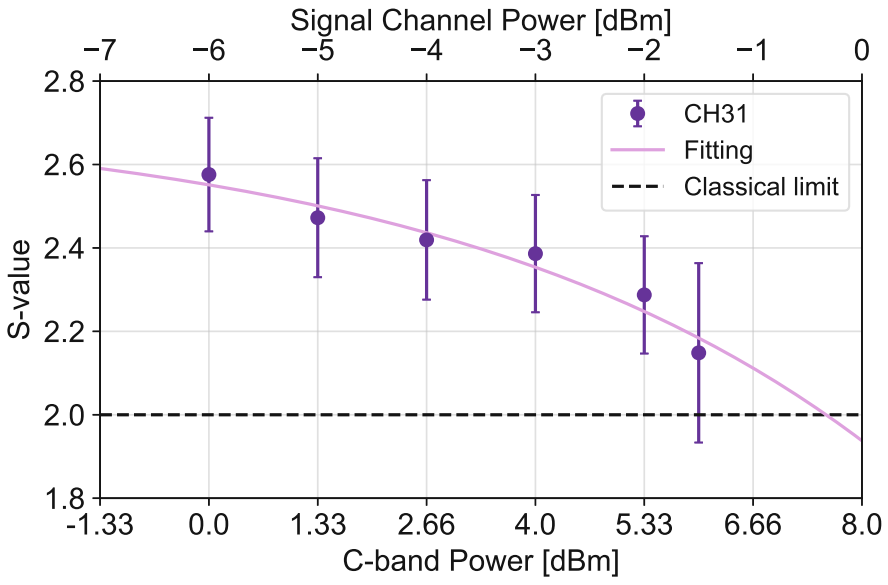

Figure 30: Measured average S-values for increasing power at the same spectral local for the classical channel.

The second aspect investigated is the impact of the spectral allocation of the classical channel. This is determined by a second experiment using the same setup as in the previous analysis but in which the total C-band power (signal and noise pedestal) is kept at a constant level of 6 dBm. The central wavelength of the classical channel is varied from CH59 (1530.3 nm, 195.9 THz) to CH24 (1558.1 nm, 192.4 THz) as shown in Figure 31.

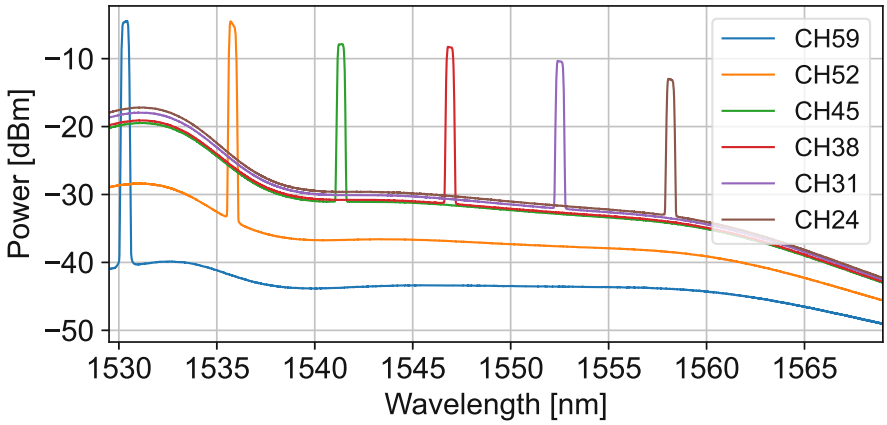

Figure 31: Transmitted optical spectra for with constant C-band power of 6 dBm. Measurement performed with a resolution bandwidth (RBW) of 0.1nm.

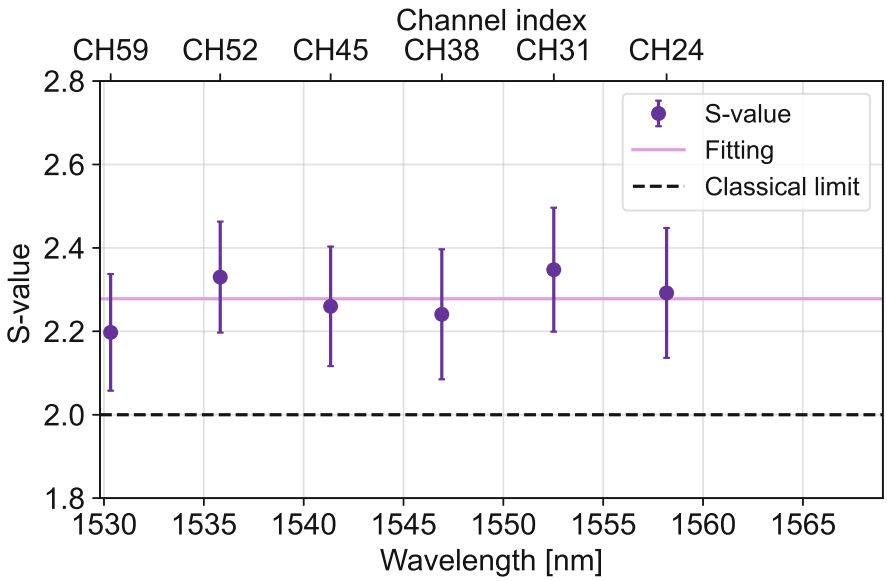

Figure 32: Measured average S-values for constant C-band power with different spectral allocation of classical channel.

No relevant change in the measured quality of the entanglement is observed, as plotted in Figure 32. To explain this behavior, it is important to note the relatively similar separations

between the quantum channel and both the nearest CH59 (206 nm) and farthest CH24 (238 nm) classical channels. Additionally, the spectral power over the whole C-Band is very broadly distributed.

In addition to quantum-classical coexistence, a hybrid network needs to operate in a stable fashion under dynamic conditions. To demonstrate robustness, dynamic routing via

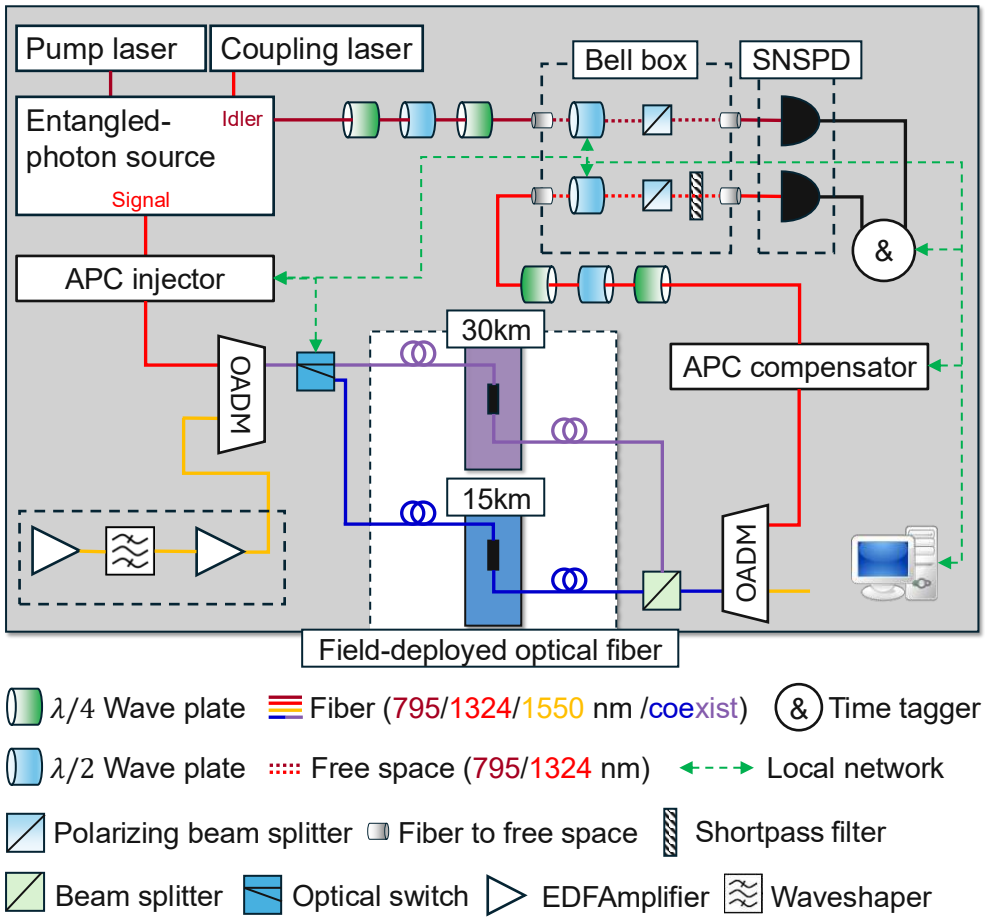

Figure 33: Experimental structure designed for multiplexing classical and quantum signals over and dynamic switching over two field deployed path.

two different deployed paths over 14 hours was performed. The optical switch periodically changes between the 15 km and 30 km fiber paths, and for each switching event a CHSH measurement is conducted. After every path switching, a compensation from the APC system is necessary. The switching experiment is repeated, with multiplexing the classical channel CH52 (1535.8 nm, 195.2 THz) into the fiber. The launch power of the classical signal to -3 dBm to guarantee its coexistence with the quantum signal while ensuring an OSNR $>$ 22 dB. For the 15 km path, an average S-value of $S_{AVG} = 2.42$ and $F_{AVG} = 86.49\%$, as for the 30 km path $S_{AVG} = 2.47$ and $F_{AVG} = 90.12\%$ as shown in Figure 34.

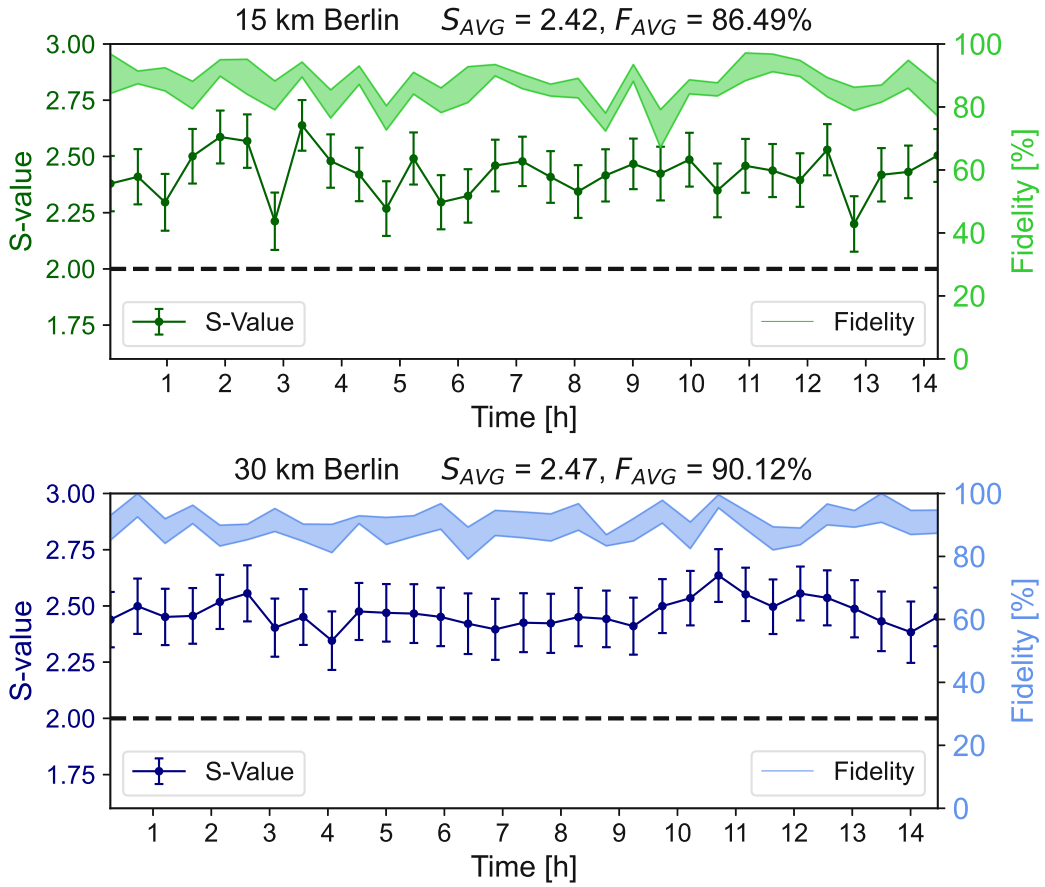

Figure 34: Path switching between 15 and 30 km path, while coexisting of classical light.

In the final phase of this work, the impact of a classical channel is investigated using a standard 50-GHz DWDM channel. An optical filter was employed to suppress the noise floor of the amplification. Illustrated in Figure 35, the 50-GHz ITU-T channel CH39 (1546.12 nm, 193.9 THz) varies in signal power from 0 dBm to 6 dBm. The total C-band power is approximately equal to the signal power, as the noise floor is effectively suppressed by the waveshaper. At the 6 dBm level, only minor rises in the noise floor are visible on each side of the signal. Intermediate signal power steps are not shown to avoid overcrowding the plot, as the noise remains similar across steps and the peak differences are minimal.

The resulting S-values as a function of signal power, illustrated in Figure 36, exhibit a trend similar to previous observations. A trade-off is evident with increasing classical signal power. In this case, entanglement verification can be demonstrated at very high signal powers.

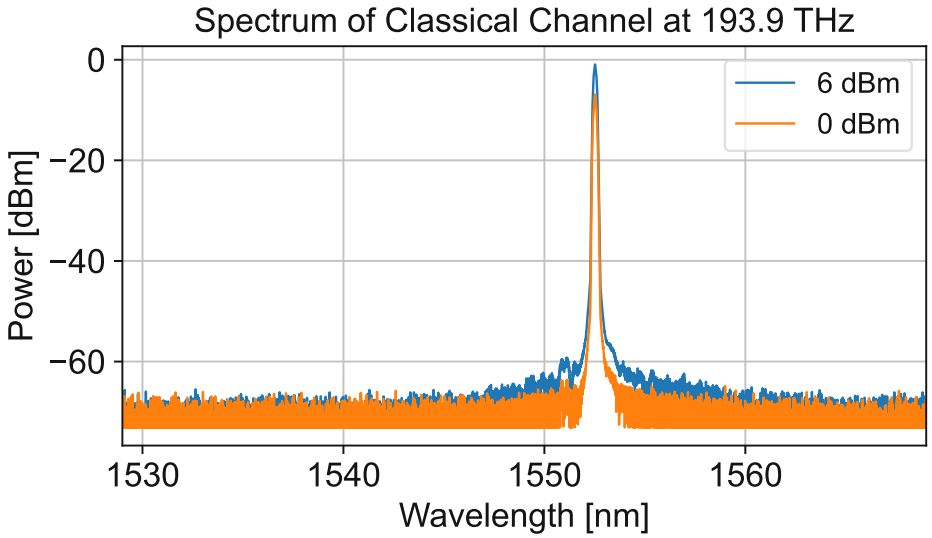

Figure 35: Optical spectrum for DWDM Channel at 193,9 THZ. Measurement performed with a resolution bandwidth (RBW) of 0.1nm.

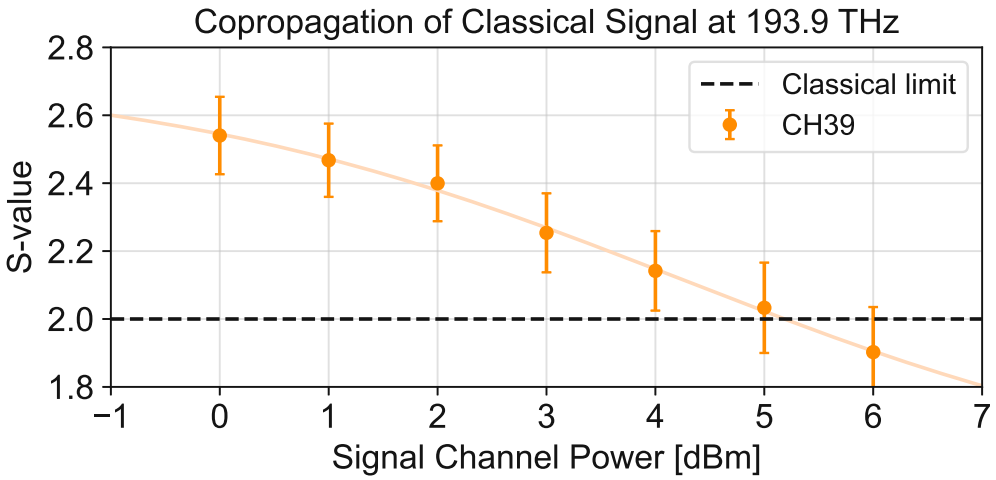

Figure 36: Measured average S-values as a function of increasing signal power on channel CH39, with background noise suppressed by spectral filtering.

6 Conclusion

This thesis has explored the feasibility of distributing, routing, and multiplexing polarization-entangled photons through an urban field-deployed fiber infrastructure owned by Deutsche Telekom AG in Berlin. The central goal was to evaluate the distribution of entanglement under real-world conditions. The experiments successfully demonstrated the distribution of O-Band polarization-encoded entangled photons. Furthermore, the impact of path switching and the coexistence of classical optical signals in the same fiber was demonstrated. The experiments were conducted in a field-deployed environment, exposing the quantum signals to environmental influences.

In the first phase, optical time-domain measurements were performed to characterize the available fiber infrastructure. Entangled photon pairs were transmitted through distances of up to 100 km, resulting in an S-value of $S = 2.49$ and fidelity between $89.82\% \leq F \leq 98.55\%$. The second phase demonstrated the impact of dynamic path switching. A controllable optical switch distributed the photons between two different paths. The importance of employing automated polarization compensation has been shown to overcome individual polarization drifts. Long-term evaluations conducted in the third phase show unpredictable polarization drifts. Without a proper polarization-maintaining mechanism, these events would mark preliminary limits. By using an automated polarization control system, it was smoothly possible to conduct experiments up to 20 hours, including path-switching events. Finally, the coexistence of O-band quantum signals with C-band classical channels was investigated. The coexistence is possible, but different effects depending on optical power and spectral allocation were observed. Classical signals tend to increase the noise and reduce the accuracy of quantum signal characterization.

In summary, this thesis confirms that field-deployed optical fiber networks can reliably support entanglement-based quantum communication, even under challenging environmental conditions.

Outlook

For the future Quantum Internet, there is great potential for further research and technological development. In particular, technologies must be improved to enable scalability and more complex network structures. For example, an automatic compensation system needs to be developed in order to make the user side (end node) as efficient as possible. This means that the device on the user side must be simple and easy to manufacture. Meanwhile, the central distribution point can host a more complex system, synchronized with the end nodes via a traditional network, or through copropagation with classical signals. Precise clock synchronization is essential, as it is a key factor in characterizing entangled photons using two different time taggers.

Bibliography

[1] H. J. Kimble. „The quantum internet“. In: *Nature* 453.7198 (2008), pp. 1023–1030. DOI: 10.1038/nature07127.

[2] C. H. Bennett, G. Brassard, and N. D. Mermin. „Quantum cryptography without Bell's theorem“. In: *Physical Review Letters* 68.5 (1992), pp. 557–559. DOI: 10.1103/PhysRevLett.68.557.

[3] H.-J. Briegel, W. Dür, J. I. Cirac, and P. Zoller. „Quantum Repeaters: The Role of Imperfect Local Operations in Quantum Communication“. In: *Phys. Rev. Lett.* 81 (1998), pp. 5932–5935. DOI: 10.1103/PhysRevLett.81.5932.

[4] C. L. Degen, F. Reinhard, and P. Cappellaro. „Quantum sensing“. In: *Reviews of Modern Physics* 89.3 (2017), p. 035002. DOI: 10.1103/RevModPhys.89.035002.

[5] J. Shi and S. Shen. „A clock synchronization method based on quantum entanglement“. In: *Scientific Reports* 12.1 (2022), p. 10185. DOI: 10.1038/s41598-022-14087-z.

[6] R. Ulrich, S. C. Rashleigh, and W. Eickhoff. „Bending-induced birefringence in single-mode fibers“. In: *Opt. Lett.* 5.6 (1980), pp. 273–275. DOI: 10.1364/OL.5.000273.

[7] M. Sena, M. Flament, M. Namazi, S. Andrewski, G. Bello, R.-P. Braun, M. Youssef-Sayed, R. Döring, M. Ritter, M. Yin, O. Holschke, and M. Geitz. „Towards the Quantum Internet: Prospects and Challenges of Efficient Entanglement Distribution Over Telecom Fibers“. In: *2024 Asia Communications and Photonics Conference (ACP) and International Conference on Information Photonics and Optical Communications (IPOC)*. 2024. DOI: 10.1109/ACP/IPOC63121.2024.10809958.

[8] M. Sena, M. Flament, S. Andrewski, I. Caltzidis, N. Bigagli, T. Rieser, G. B. Portmann, R. Sekelsky, R.-P. Braun, A. N. Craddock, M. Schulz, K. D. Jöns, M. Ritter, M. Geitz, O. Holschke, and M. Namazi. *High-Fidelity Quantum Entanglement Distribution in Metropolitan Fiber Networks with Co-propagating Classical Traffic*. 2025. arXiv: 2504.08927 [quant-ph]. URL: https://arxiv.org/abs/2504.08927.

[9] D. F. V. James, P. G. Kwiat, W. J. Munro, and A. G. White. „Measurement of qubits“. In: *Physical Review A* 64 (2001), p. 052312. DOI: 10.1103/PhysRevA.64.052312.

[10] I. Marcikic, H. De Riedmatten, W. Tittel, H. Zbinden, M. Legré, and N. Gisin. „Distribution of time-bin entangled qubits over 50 km of optical fiber“. In: *Physical review letters* 93.18 (2004), p. 180502.

[11] L. Shen, C. H. Chow, J. Y. X. Peh, X. J. Yeo, P. K. Tan, and C. Kurtsiefer. „Distributing Polarization-Entangled Photon Pairs with High Rate Over Long Distances through Standard Telecommunication Fiber“. In: *Phys. Rev. Appl.* 18 (2022), p. 044075. DOI: 10.1103/PhysRevApplied.18.044075.

[12] J. M. Thomas, F. I. Yeh, J. H. Chen, J. J. Mambretti, S. J. Kohlert, G. S. Kanter, and P. Kumar. „Quantum teleportation coexisting with classical communications in optical fiber“. In: *Optica* 11.12 (2024), pp. 1700–1707. DOI: 10.1364/OPTICA.540362.

[13] Y. Mao, B.-X. Wang, C. Zhao, G. Wang, R. Wang, H. Wang, F. Zhou, J. Nie, Q. Chen, Y. Zhao, Q. Zhang, J. Zhang, T.-Y. Chen, and J.-W. Pan. „Integrating quantum key distribution with classical communications in backbone fiber network“. In: *Opt. Express* 26.5 (2018), pp. 6010–6020. DOI: 10.1364/OE.26.006010.

[14] T. Strobel, S. Kazmaier, T. Bauer, M. Schäfer, A. Choudhary, N. L. Sharma, R. Joos, C. Nawrath, J. H. Weber, W. Nie, G. Bhayani, L. Wagner, A. Bisquerra, M. Geitz, R.-P. Braun, C. Hopfmann, S. L. Portalupi, C. Becher, and P. Michler. „High-fidelity distribution of triggered polarization-entangled telecom photons via a 36 km intra-city fiber network“. In: *Optica Quantum* 2.4 (2024), pp. 274–281. DOI: 10.1364/OPTICAQ.530838.

[15] A. N. Craddock, A. Lazenby, G. B. Portmann, R. Sekelsky, M. Flament, and M. Namazi. „Automated distribution of polarization-entangled photons using deployed new york city fibers“. In: *PRX Quantum* 5.3 (2024), p. 030330.

[16] S. Kucera, C. Haen, E. Arenskötter, T. Bauer, J. Meiers, M. Schäfer, R. Boland, M. Yahyapour, M. Lessing, R. Holzwarth, C. Becher, and J. Eschner. *Demonstration of quantum network protocols over a 14-km urban fiber link*. 2024. arXiv: 2404.04958 [quant-ph]. URL: https://arxiv.org/abs/2404.04958.

[17] B. Schumacher. „Quantum coding“. In: *Phys. Rev. A* 51 (1995), pp. 2738–2747. DOI: 10.1103/PhysRevA.51.2738.

[18] P. Dirac. *The Principles of Quantum Mechanics*. Clarendon Press, 1981. URL: https://books.google.de/books?id=XehUpGiM6FIC.

[19] P. A. M. Dirac. „A new notation for quantum mechanics“. In: *Mathematical Proceedings of the Cambridge Philosophical Society* 35.3 (1939), pp. 416–418. DOI: 10.1017/S0305004100021162.

[20] R. P. Feynman, F. L. Vernon Jr, and R. W. Hellwarth. „Geometrical representation of the Schrödinger equation for solving maser problems“. In: *Journal of applied physics* 28.1 (1957), pp. 49–52.

[21] A. Tchebotareva, S. L. Hermans, P. C. Humphreys, D. Voigt, P. J. Harmsma, L. K. Cheng, A. L. Verlaan, N. Dijkhuizen, W. de Jong, A. Dréau, and R. Hanson. „Entanglement between a Diamond Spin Qubit and a Photonic Time-Bin Qubit at Telecom Wavelength“. In: *Physical Review Letters* 123.6 (2019). DOI: 10.1103/physrevlett.123.063601.

[22] N. Tagliavacche, M. Borghi, G. Guarda, D. Ribezzo, M. Liscidini, D. Bacco, M. Galli, and D. Bajoni. „Frequency-bin entanglement-based Quantum Key Distribution“. In: *npj Quantum Information* 11.1 (2025). DOI: 10.1038/s41534-025-00991-5.

[23] A. I. Lvovsky, B. C. Sanders, and W. Tittel. *Optical quantum memory*. 2010. arXiv: 1002.4659 [quant-ph]. URL: https://arxiv.org/abs/1002.4659.

[24] R. C. Jones. „A New Calculus for the Treatment of Optical SystemsI. Description and Discussion of the Calculus“. In: *J. Opt. Soc. Am.* 31.7 (1941), pp. 488–493. DOI: 10.1364/JOSA.31.000488.

[25] G. G. Stokes. „On the Composition and Resolution of Streams of Polarized Light from different Sources“. In: *Mathematical and Physical Papers*. Cambridge Library Collection - Mathematics. Cambridge University Press, 2009, pp. 233–258.

[26] R. Horodecki, P. Horodecki, M. Horodecki, and K. Horodecki. „Quantum entanglement“. In: *Reviews of Modern Physics* 81.2 (2009), pp. 865–942. DOI: 10.1103/revmodphys.81.865.

[27] A. M. Fox. *Quantum optics: an introduction*. Oxford university press, 2006.

[28] J. S. Bell. „On the Einstein Podolsky Rosen paradox“. In: *Physics Physique Fizika* 1 (1964), pp. 195–200. DOI: 10.1103/PhysicsPhysiqueFizika.1.195.

[29] R. W. Boyd, A. L. Gaeta, and E. Giese. „Nonlinear Optics“. In: *Springer Handbook of Atomic, Molecular, and Optical Physics*. Ed. by G. W. F. Drake. Cham: Springer International Publishing, 2023, pp. 1097–1110. ISBN: 978-3-030-73893-8. DOI: 10.1007/978-3-030-73893-8_76. URL: https://doi.org/10.1007/978-3-030-73893-8_76.

[30] S. Walborn, C. Monken, S. Pádua, and P. Souto Ribeiro. „Spatial correlations in parametric down-conversion“. In: *Physics Reports* 495.4–5 (2010), pp. 87–139. DOI: 10.1016/j.physrep.2010.06.003.

[31] A. N. Craddock, Y. Wang, F. Giraldo, R. Sekelsky, M. Flament, and M. Namazi. „High-rate subgigahertz-linewidth bichromatic entanglement source for quantum networking“. In: *Physical Review Applied* 21 (2024), p. 034012. DOI: 10.1103/PhysRevApplied.21.034012.

[32] H. Wang, H. Hu, T.-H. Chung, J. Qin, X. Yang, J.-P. Li, R.-Z. Liu, H.-S. Zhong, Y.-M. He, X. Ding, Y.-H. Deng, Q. Dai, Y.-H. Huo, S. Höfling, C.-Y. Lu, and J.-W. Pan. „On-Demand Semiconductor Source of Entangled Photons Which Simultaneously Has High Fidelity, Efficiency, and Indistinguishability“. In: *Physical Review Letters* 122.11 (2019). DOI: 10.1103/physrevlett.122.113602.

[33] A. K. Ekert. „Quantum cryptography based on Bell's theorem“. In: *Phys. Rev. Lett.* 67 (1991), pp. 661–663. DOI: 10.1103/PhysRevLett.67.661.

[34] A. Einstein, B. Podolsky, and N. Rosen. „Can Quantum-Mechanical Description of Physical Reality Be Considered Complete?“ In: *Phys. Rev.* 47 (1935), pp. 777–780. DOI: 10.1103/PhysRev.47.777.

[35] A. Einstein, M. Born, and H. Born. *The Born-Einstein Letters: Correspondence Between Albert Einstein and Max and Hedwig Born from 1916-1955, with Commentaries by Max Born*. Macmillan, 1971. URL: https://books.google.de/books?id=HvZAAQAAIAAJ.

[36] J. F. Clauser, M. A. Horne, A. Shimony, and R. A. Holt. „Proposed experiment to test local hidden-variable theories“. In: *Physical Review Letters* 23.15 (1969), p. 880. DOI: 10.1103/PhysRevLett.23.880.

[37] B. S. Cirel'son. „Quantum generalizations of Bell's inequality". In: *Letters in Mathematical Physics* 4.2 (1980), pp. 93–100. DOI: 10.1007/BF00417500.

[38] C. M. Natarajan, M. G. Tanner, and R. H. Hadfield. „Superconducting nanowire single-photon detectors: physics and applications". In: *Superconductor Science and Technology* 25.6 (2012), p. 063001. DOI: 10.1088/0953-2048/25/6/063001.

[39] M. Brodsky, N. J. Frigo, M. Boroditsky, and M. Tur. „Polarization Mode Dispersion of Installed Fibers". In: *Journal of Lightwave Technology* 24.12 (2006), pp. 4584–4599. DOI: 10.1109/JLT.2006.885781.

[40] M. Sena, M. Flament, M. Namazi, S. Andrewski, G. Portmann, R.-P. Braun, M. Youssef-Sayed, R. Döring, M. Ritter, O. Holschke, et al. „High-Fidelity Entanglement Distribution Through Berlin Using an Operator's Fiber Infrastructure". In: *Optical Fiber Communication Conference*. Optica Publishing Group. 2025.

[41] T. Rieser, M. Sena, S. Andrewski, B. Niccolò, M. Flament, R.-P. Braun, M. Ritter, M. Namazi, and M. Geitz. „Distributing, Routing and Multiplexing O-Band Polarization-Entangled Photons with C-Band Classical Light over an Operator's Metropolitan Fiber Network". In: *2025 European Conference on Optical Communications (ECOC)*. 2025.